Methods to introduce floating bridge motion and wind excitation on a model for the investigation of heavy vehicle dynamics

Citation for the original published paper (version of record):
Sivaramakrishnan, P., Madhava Prakash, A., Sekulic, D. et al (2023). Methods to introduce floating bridge motion and wind excitation on a model for the
investigation of heavy vehicle dynamics. Applied Mathematical Modelling, 117: 118-141.
http://dx.doi.org/10.1016/j.apm.2022.11.038

Applied Mathematical Modelling 117 (2023) 118–141

Contents lists available at ScienceDirect

Applied Mathematical Modelling

journal homepage: www.elsevier.com/locate/apm

Methods to introduce floating bridge motion and wind excitation on a model for the investigation of heavy vehicle dynamics

Pramod Sivaramakrishnan[a], Ajit Kumar Madhava Prakash[a], Dragan Sekulic[a,1,*], Bengt Jacobson[a], Cihan Selvi[b], Stian Moe Johannesen[c]

[a] Chalmers University of Technology, Gothenburg, Sweden
[b] Hexagon Manufacturing Intelligence, Gothenburg, Sweden
[c] The Norwegian Public Roads Administration, Oslo, Norway

ARTICLE INFO

Article history:
Received 30 November 2021
Revised 25 November 2022
Accepted 29 November 2022
Available online 12 December 2022

Keywords:
Floating bridge
Wind loads
Lateral stability
Vehicle safety
Tractor semi-trailer modelling
Vehicle aerodynamics

ABSTRACT

The proposed floating bridge solution at Bjørnafjorden in connection with the E39 infrastructure upgrade is an enabler to realize efficient transportation. This bridge and the vehicles shuttling on it will be exposed to inclement weather conditions. The waves and wind excite the floating bridge to induce compound motion in addition to the aerodynamic crosswinds directly interacting with the vehicles. Methods to introduce the complex motion of the floating bridge (multi-post test rig) and aerodynamic crosswinds on a tractor semi-trailer have been established and presented in this paper. The environment-vehicle-driver system is enabled through a co-simulation between MATLAB/Simulink (primary) and Adams (secondary). This complex interplay is studied on the intricate 627-DoF Adams vehicle model coupled with the Adams driver model. Numerical simulations are performed for multiple constant vehicle speeds under laden condition on a road with friction of 0.7 for the 1-year storm weather condition. Vehicle stability and safety assessments such as lane violation, path following ability, rollover risk, and lateral side slip limit are evaluated to draw inferences. Subsequently, permissible vehicle speed for a laden tractor semi-trailer to operate on the floating bridge is suggested. Furthermore, a simpler 9-DoF tractor semi-trailer vehicle model developed in MATLAB/Simulink combined with the pure pursuit tracking based driver model is compared with the Adams model under identical environmental conditions for an unladen case. The simpler vehicle-driver model is validated against the detailed Adams vehicle-driver model through numerical simulations for different constant vehicle speeds.

* Corresponding author.
E-mail addresses: prasiv@net.chalmers.se (P. Sivaramakrishnan), ajit@net.chalmers.se (A.K. Madhava Prakash), dragan.sekulic@chalmers.se (D. Sekulic), bengt.jacobson@chalmers.se (B. Jacobson), cihan.selvi@hexagon.com (C. Selvi), stian.moe.johannesen@vegvesen.no (S.M. Johannesen).
[1] d.sekulic@sf.bg.ac.rs

https://doi.org/10.1016/j.apm.2022.11.038

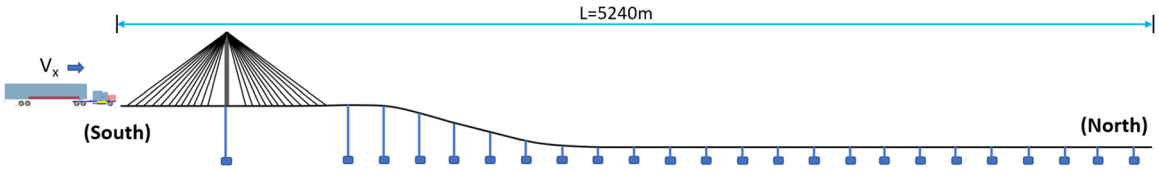

Fig. 1. Bjørnafjorden floating bridge.

1. Introduction

The European route E39 is undergoing an upgrade for a more sustainable commute between northern Denmark and northern Norway. The Norwegian part of the highway spans 1100 km along the western coast, between the cities of Kristiansand and Trondheim. This comprises of several ferry-crossings and currently takes approximately 21 hours to commute. The aim of Norwegian Public Roads Administration (NPRA) is to make this route a ferry-free highway, thereby reducing travel time. This is expected to contribute to the economic development of smaller cities along the Norwegian west coast [1].

One such ferry-free crossing is at Bjørnafjorden, which spans approximately 5 km. The proposed solution for this crossing is a pontoon floating bridge (Fig. 1) [2,3]. Vehicular traffic along this bridge is subject to gusty winds and wet/icy road surface during extreme weather, in addition to bridge motion excitations (heave, roll and lateral movements). Determining safe operating speeds for traffic in such conditions is paramount. A high-sided vehicle such as a tractor semi-trailer has a large surface area which is susceptible to crosswinds. It is therefore important to study the vehicle dynamics and responses of such vehicles under adverse environmental conditions [4].

Two vehicle models with 13 DoF [5], (a light truck and a passenger car) travelling on a slender coastal bridge were evaluated with respect to their ride comfort and driving safety. It was seen that when these vehicles are subjected to both wind and wave excitation, effect of wave is far less than the effect of wind on the overall ride comfort, roll and side slip safety. Investigation indicated that the effects of wave on the overall vibration total values, the roll safety criteria and the sideslip safety criteria are much less than those from the wind. Also, a high-sided vehicle model with 11 DoF travelling over a slender arch bridge under turbulent wind was investigated for driving safety and ride comfort [6]. It was shown that bridge vibration, specifically peak acceleration and frequency content is significantly affected by the crosswind while it also has significant effect on the ride comfort in lateral direction which can lead to overturning accidents. Another study was made on the safety analysis of a high-sided vehicle model with 19 DoF travelling over a long span cable-stayed bridge oscillating under sharp edged crosswind [7]. Study shows that these crosswind induced oscillations decreases the accident vehicle speed if the wind speed goes beyond a critical level.

Numerical simulations as well as driving simulator are utilized to investigate the significance of vertical floating bridge excitation on ride comfort and road grip of a bus with multiple vehicle longitudinal speeds [8]. The research highlighted that the weighted vertical accelerations were slightly uncomfortable at 76 km/h speed. The poor road grip was attributed to higher dynamic load coefficient at higher speeds. Driver-in-loop studies were performed using the passenger car and bus vehicle models on a driving simulator for low to high intensity weather conditions [8–11]. Overtaking and lane changing maneuvers were observed to be difficult in high intensity weather when compared to that of a low intensity weather condition. Additionally, the effect of the floating bridge on driving behaviour was investigated. It was concluded that the lane keeping for the bus was more difficult than that of the passenger car.

Research on a passenger car, intercity bus, and tractor semi-trailer (TS) pertaining to the Bjørnafjorden floating bridge have been carried out in the past [4,9,12]. A relatively simple TS model, with 9 DoF, for investigation of its dynamic behaviour on floating bridge was defined in MATLAB/Simulink software [12]. Model incorporates linear spring/damper characteristics of the suspension systems and non-linear brush tyre model. Floating bridge motions and wind excitations were introduced in the TS model by imported procedure already established in MATLAB software. Unlike the paper [12], current work aims to developed two novel methods for importing moving ground motions and wind excitations in ADAMS Car Truck software. More specifically, methods are based on multi-test post rig in ADAMS and on co-simulation of aerodynamic loads from MATLAB with multibody model. These new ADAMS software tools could certainly broaden existing simulation possibilities when it comes to investigation of dynamics behaviour of complex vehicle models.

Assessments such as lateral lane deviation, rollover risk and steering effort for the TS were determines across various test speeds, semi-trailer payload and road surface friction [4]. Results from that unpublished research of current authors is included in this paper. Additionally, this paper further develops the moving-ground excitation method compared to the extensive study conducted on the vehicle dynamics behaviour of a detailed TS model in the masters thesis [4].

Historically, speed limits on bridges in extreme weather conditions are determined based on intuition and past experiences [13]. Each experience applies to a specific bridge under a specific weather condition. Therefore, a model based assessment would be much more useful in determining speed limits for vehicles. First, this paper aims to establish methods to introduce floating bridge motion and wind gust excitations for investigating the TS's lateral dynamic responses using Adams Car Truck module. Secondly, a simpler TS model previously built in MATLAB/Simulink software is validated. Finally, the goal

Table 1
Vehicle attributes - Adams TS model.

Sub-system	Type
Tractor	Rigid body cab, frame and fifth wheel sub-assembly
Steering	Re-circulating ball pitman arm steering
Steer axle suspension	Leaf spring suspension with dampers
Tractor axles	Solid twin axle suspension with dampers
Semi-trailer	Rigid body trailer with 17.1 ton payload
Semi-trailer axles	Coil spring suspension with dampers
Tyres	PAC2002 Tyre model

Table 2
Axle loading condition - Adams TS model.

Axle	Laden [ton]	Unladen [ton]
1: Front axle	5.70	5.32
2: First driven axle	7.84	3.88
3: Second driven axle	7.92	3.08
4: First semi-trailer axle	7.45	3.52
5: Second semi-trailer axle	7.40	3.40

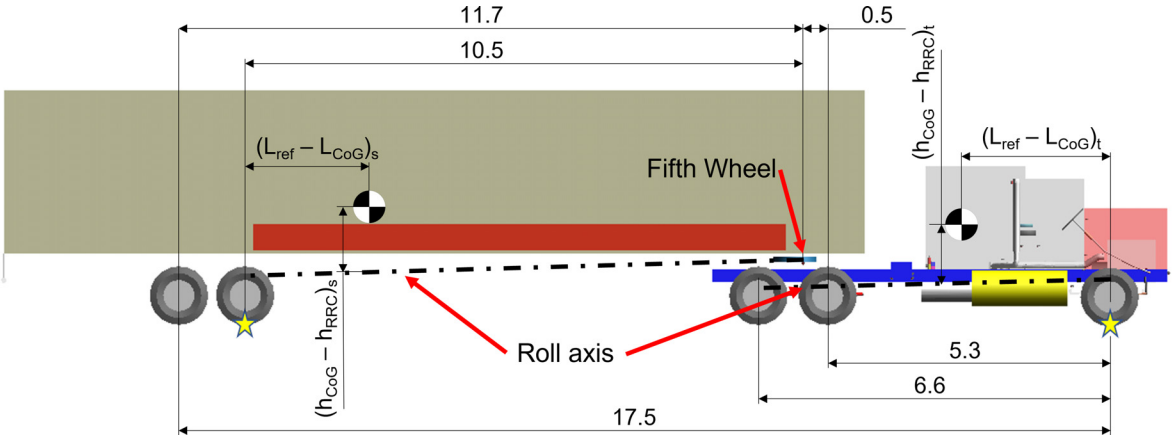

Fig. 2. Vehicle dimensions used in Adams TS model (all dimensions in m).

is to provide insights regarding the safe operating speeds of a TS on a dry/wet road surface (μ=0.7), in a 1-year storm condition.

2. Vehicle model - Adams Car Truck

Multi-body vehicle dynamics models have often been used in numerical simulation when investigating different problems for vehicle longitudinal, lateral, and vertical dynamics behavior [14,15]. The vehicle model considered for this research is based on the detailed TS vehicle model from Adams *shared_truck* database. The model has an overall wheelbase of 17.5 m, height of 5.7 m and track width of 2.55 m. The tractor unit contains a rigid chassis and a fifth wheel coupling. The tractor and semi-trailer units are connected through the fifth wheel. The Adams vehicle model has 190 moving parts, 19 subsystems and 627 DoF. Details of sub-systems used in the TS model are described in Tab. 1. The loads on each of the 5 axles (1 steered axle, 2 drive axles on the tractor unit, 2 trailer axles and consisting 18 wheels) are listed in Tab. 2. The mass of the tractor and the semi-trailer units are 10.8 ton and 8.4 ton, respectively. With a payload of 17.1 ton, the semi-trailer weighs 25.5 ton. The laden and unladen gross vehicle weight is 36.3 ton and 19.2 ton respectively. Significant vehicle dimensions of the Adams TS model are illustrated in Fig. 2.

3. Driver model

3.1. Pure pursuit method

The pure pursuit method based driver model is applied in this work [16]. This technique defines a measure of error between the look ahead distance preceding the vehicle and the intended path to determine control law solutions using

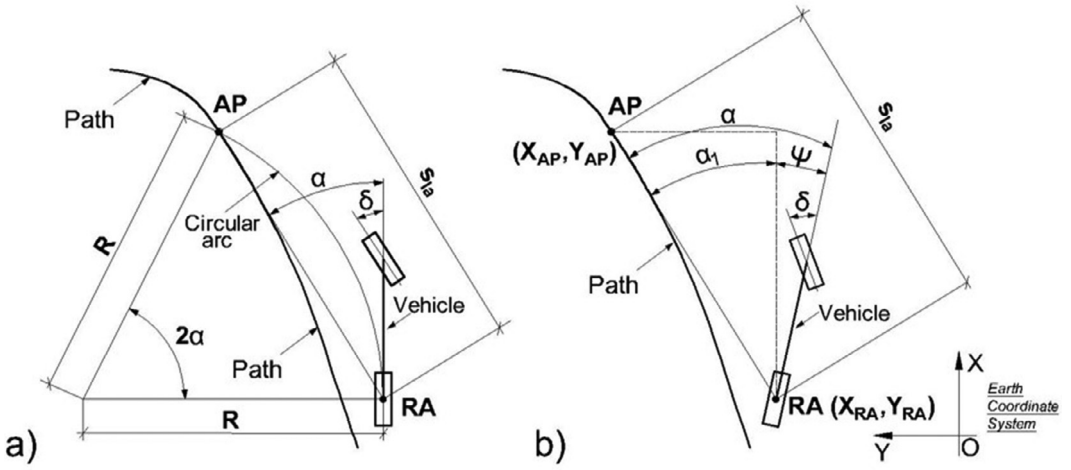

Fig. 3. a) Pure Pursuit Geometry; b) Positions of the characteristic points and angles [16], [9].

geometric relationships. The vehicle motion is assumed to follow ideal-tracking tyres, i.e., zero sideslip independent of forces [9].

The aim point (X_{AP}, Y_{AP}) on the desired path and the midpoint of the vehicle's rear axle (X_{RA}, Y_{RA}) have been determined (Fig. 3). A look-ahead distance s_{la} is considered from the rear-axle position when computing the location of the aim point to calculate the angle α:

$$\alpha = \alpha_1 + \psi = \sin^{-1}\left(\frac{Y_{AP}-Y_{RA}}{s_{la}}\right) + \psi \tag{1}$$

where ψ is the yaw angle of the vehicle. The steering angle δ is established using the angle α and the location of the aim point such that

$$\delta = \left(\frac{2L\alpha}{s_{la}}\right) = \left(\frac{2L\alpha}{t_{la}\cdot v_x}\right) \tag{2}$$

where α is the angle between the vehicle's heading direction and the look-ahead vector; L is the wheelbase of the vehicle; t_{la} is the preview time; and v_x is the constant vehicle longitudinal speed. The handwheel steering angle (HSA) is consequently calculated through the steering ratio.

3.2. Machine control - Adams

Machine Control is a vehicle controller that simulates a driver's control actions [17]. This control action integrates a reference trajectory planner and a model-predictive controller (MPC), also called as a feed-forward plus feedback controller. Machine control implements these estimated controls as feed-forward inputs without delay. Feedback controllers (δ_{FB}), which is the yaw rate controller, continuously correct differences occurring between the behaviour of the simulated vehicle and the expected behaviour of the idealized models, to alter the control actions in order to minimize this error.

3.2.1. Feed-Forward lateral control

A bicycle model (Fig. 4a) is used for the simulated vehicle through which the lateral control action's feed-forward component (δ_{FF}) is calculated. The simplicity of the bicycle model allows the analytical identification of the relationship between the geometry of the intended path and the required control action (steering angle). Furthermore, the lateral tyre forces from both wheels on an axle are assumed to act in the same direction, and the left and right steer angles are assumed to be the same. That is, Ackermann steering geometry is not considered. Consequently, the tyres are lumped together into a single tyre representation, and the model is commanded by a single steer angle.

3.2.2. Trajectory control - Connecting contour

For the lateral control of the vehicle with a target path, a bicycle model representation of the vehicle (Fig. 4a) is used to compute the control action that should cause the vehicle to follow the intended path. The simulated vehicle, however, may not exactly follow the target path because of differences between the simplified model and the simulated vehicle, or external factors (road roughness and aerodynamic disturbances) and therefore some manual fine tuning of control parameters might be needed. Therefore, the potential for offset between the instantaneous vehicle location and heading, and the location and heading of the path must be considered. In considering the location and heading of the path, Machine Control builds a connecting contour (maroon curve, Fig. 4b) between the current vehicle position (wherever it may be) and some point on the target path (blue curve, Fig. 4b), along which the vehicle will be steered to later bring it back to the target path, where,

D (Preview distance) ⇒ distance ahead from the current vehicle (gyro point) position to the preview point.

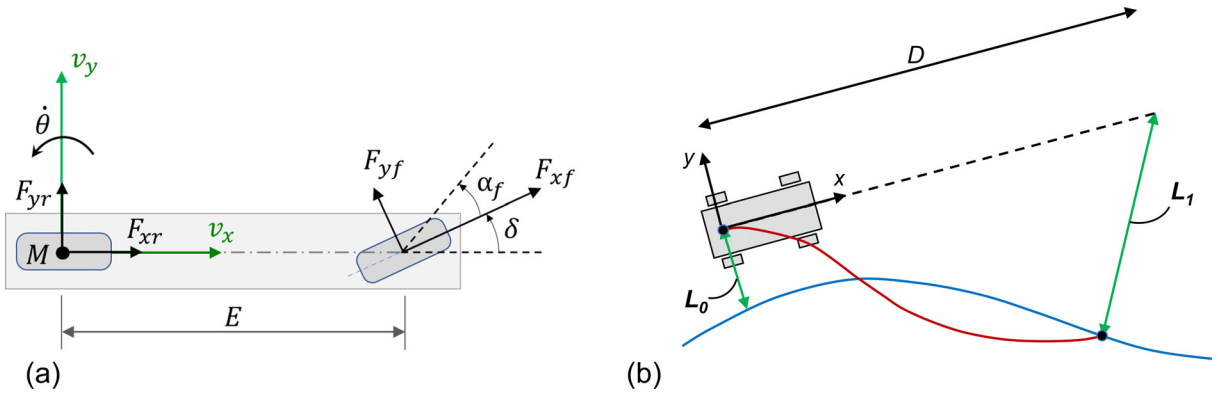

Fig. 4. a) Bicycle Model [17] b) Connecting Contour [17].

L_0 (Path distance) ⇒ distance from current vehicle (gyro point) position to the nearest point on the path, projected on the road surface.

L_1 (Preview-point distance) ⇒ distance from preview point to the nearest point on the path, projected on the road surface.

The function that describes the connecting contour is parameterized such that one end of the connecting contour matches the position and direction of the vehicle (at the vehicle rear axle) and the other end of the connecting contour matches the path (at the preview distance, where the contour connects with the target path), as shown in the (Fig. 4b). The most effective adjustment to the connecting contour is the preview distance, which is typically controlled by changing the preview time. The connecting contour then becomes the reference trajectory (path) for the lateral control of the vehicle, and the vehicle is steered by both feed-forward and feedback controllers, such that it should follow this connecting contour. The connecting contour is updated each time the Machine Control controller is called.

3.2.3. Lateral displacement feedback (path distance compensation)

The connecting contour approach does not include any term to correct for steady-state lateral displacement error. This is preferred in most situations, because the resulting control actions tend to be more realistic and robustly stable. Once the vehicle is close to the target path, an additional controller acting on the distance L_0 (path distance) adjusts the lateral displacement of the vehicle:

$$\delta_{LDC} = K_{LDC} \cdot \int_0^t f_{LDC} L_0 \, dt \tag{3}$$

where f_{LDC} is a flag indicating whether the lateral displacement controller is activated, that is whether the lateral displacement error L_0 is small, and K_{LDC} is the lateral displacement controller's gain.

3.2.4. Summation of feed-forward and feedback terms

A simple summation of the feed-forward and feedback terms gives the total demand from the lateral controller for steer angle:

$$\delta = \delta_{FF} + \delta_{FB} + \delta_{LDC} \tag{4}$$

where,

δ_{FF} : feed-forward component of the steering demand from the bicycle model
δ_{FB} : feedback predictive yaw rate controller component of the steering demand
δ_{LDC} : lateral displacement compensation component of the steering demand

3.3. Driver model comparison

The Pure Pursuit Controller (PPC) [16] and Adams driver model are compared using the detailed Adams vehicle model with a fully loaded trailer travelling at 36 km/h, on a road with friction μ=0.7. The outcome of preliminary simulations for a Preview Time of 0.4 *s* were observed to be numerically stable.

Fig. 5 a presents the HSA for the Adams driver model and the PPC. The HSA signals from the PPC are observed to be volatile compared to the Adams controller, although they appear to oscillate about a similar mean value.

The signal intensities of the HSA produced in the frequency domain are illustrated as Power Spectral Density (PSD) in Fig. 5b. The first noteworthy observation is the similarity between the PPC and Adams driver model up to the frequency of 0.15 Hz (region highlighted in yellow). The peak magnitude of the signal intensities in this region correspond to the steering corrections arising due to the crosswind disturbances represented in Fig. 15c.

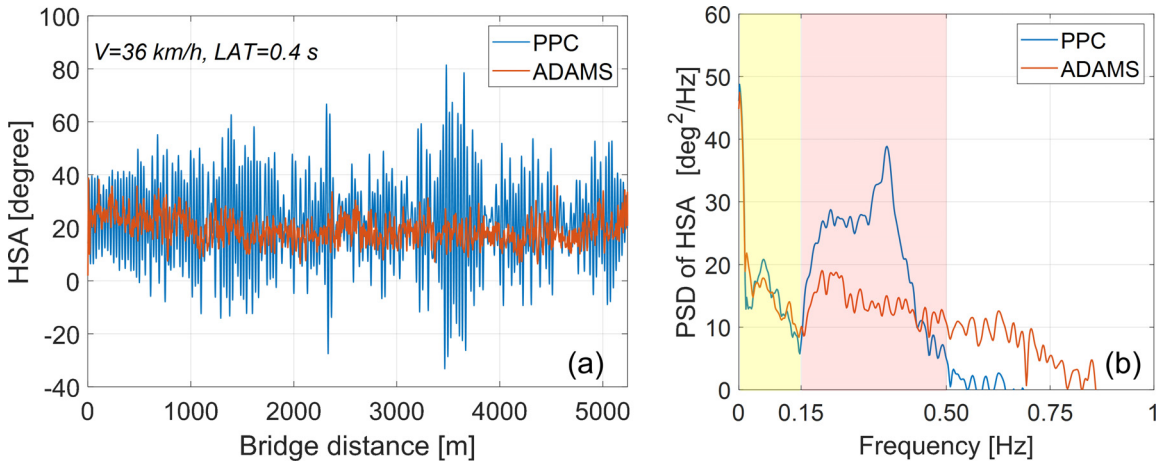

Fig. 5. HSA signals a) for laden vehicle b) in frequency domain.

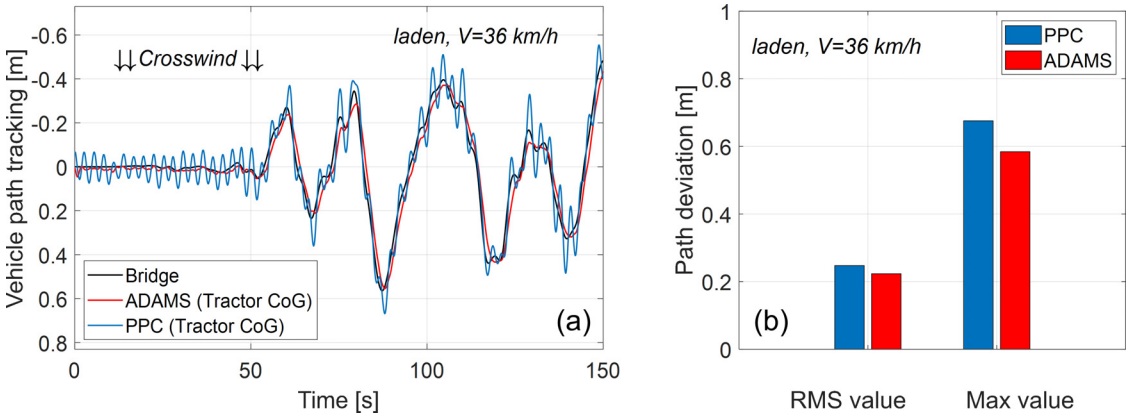

Fig. 6. a) Path tracking ability b) Path deviation parameters.

The signal intensities concentrated between 0.15 Hz and 0.50 Hz (region highlighted in red) in Fig. 5b correspond to the steering corrections consequent to the path-following (Fig. 6a) aspect of the driver model. The magnitude of the signal intensities vary at these frequencies and this difference is due to the inherent design of the two driver models. While the HSA calculations in the PPC model relies purely on the geometric relationship, the Adams driver model which is also based on the similar concept is embedded within a PID controller that accounts for the error feedback. Additionally, the PID controller compensates for the lateral path offset between the vehicle and the desired path.

The path tracking ability of the driver models are illustrated in Fig. 6a. A small lateral offset between the desired path on the bridge and the tractor's center of gravity (CoG) has been observed with the PPC under similar conditions [9], as this driver model does not account for the effect of crosswind disturbance on the vehicle's lateral offset while computing the HSA. In reality, the driver compensates for the lateral offset by steering the vehicle back to the intended path under the influence of crosswind disturbances acting on the vehicle [9]. Therefore, on removing this lateral offset from the vehicle path to compare with the path from Adams' driver model, it is noticed that path tracking ability of both the driver models are comparable. Furthermore, the path deviation parameters are also observed to be rather close (Fig. 6b).

Acknowledging the differences but owing to the similarities existing between the steering amplitudes centred around similar frequencies (Fig. 5b), and to the equivalence observed in the path tracking abilities (Fig. 6a and Fig. 6b), the two driver models are decided to be used interchangeably. The advanced controller Adams driver model will be used in conjunction with the detailed Adams vehicle model, while the simpler PPC will be used together with the vehicle model implemented in MATLAB/Simulink to investigate and draw comparisons with for different test cases.

4. Definition of the methods

The TS vehicle experiences excitation from bridge motion and wind gusts. This section of the paper describes the methods established to simultaneously induce bridge motion and wind excitation on the TS model. The data considered for this research is from a 1-year storm condition simulated on *WindSim* software. The input disturbance is available in the form

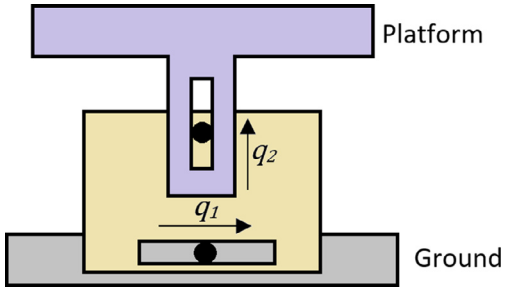

Fig. 7. Schematic representation of the test rig.

Table 3
Denavit-Hartenberg's kinematic parameters.

$Link_i$	**Joint angle** (θ_i)	Link offset (d_i)	Link length (a_i)	Link twist (α_i)
1	0	q_1	0	0
2	0	q_2	0	- $\pi/2$

of bridge motion displacement and wind velocity, as a function of time and location on the bridge. The data set is chosen such that the vehicle experiences the highest RMS value of the lateral wind velocity during its journey in the South-North direction [4,9].

4.1. Method to introduce floating bridge motion excitation

The method to introduce floating bridge motion excitation includes a test-rig modelled as *Cartesian manipulator* which has a vertical and horizontal displacement (Fig. 7). Two translation (prismatic) joints are used in order to model the vertical and horizontal bridge excitation on each vehicle wheel (wheels on either tracks on every axle).

Denavit Hartenberg parameters associated with joint 1 and joint 2 are listed in Table 3.

Each homogeneous transformation is described in the Denavit Hartenberg method as [18]

$$A_i = R_{z,\theta_i} \cdot T_{z,d_i} \cdot T_{x,a_i} \cdot R_{x,\alpha_i} \tag{5}$$

where,

R_x is the rotational transformation matrix around x-axis.
R_z is the rotational transformation matrix around z-axis.
T_x is the translational transformation matrix around x-axis.
T_z is the translational transformation matrix around z-axis.

For prismatic joints, the Jacobian matrix and its linear and angular components can be derived as:

$$J = \begin{bmatrix} J_v \\ J_w \end{bmatrix}, J_{v,i} = z_{i-1} \qquad and \quad J_{w,i} = 0 \tag{6}$$

where,

J_v is the linear component of the Jacobian matrix for joint 1 or joint 2.
J_w is the angular component of the Jacobian matrix for joint 1 or joint 2.

$$J_{v_1} = \begin{bmatrix} z_0 & 0 \end{bmatrix} = \begin{bmatrix} 1 & 0 \\ 0 & 0 \\ 0 & 0 \end{bmatrix}, \qquad J_{v_2} = \begin{bmatrix} z_0 & z_1 \end{bmatrix} = \begin{bmatrix} 1 & 0 \\ 0 & 0 \\ 0 & 1 \end{bmatrix} \tag{7}$$

Velocity components can be expressed as:

$$v_1 = [J_{v_1}] \begin{bmatrix} \dot{q}_1 \\ \dots \\ \dot{q}_2 \end{bmatrix} = \begin{bmatrix} 1 \\ 0 \\ 0 \end{bmatrix} \dot{q}_1 + \begin{bmatrix} 0 \\ 0 \\ 0 \end{bmatrix} \dot{q}_2 = \begin{bmatrix} \dot{q}_1 \\ 0 \\ 0 \end{bmatrix} \tag{8}$$

$$v_2 = [J_{v_2}] \begin{bmatrix} \dot{q}_1 \\ \dots \\ \dot{q}_2 \end{bmatrix} = \begin{bmatrix} 1 \\ 0 \\ 0 \end{bmatrix} \dot{q}_1 + \begin{bmatrix} 0 \\ 0 \\ 1 \end{bmatrix} \dot{q}_2 = \begin{bmatrix} \dot{q}_1 \\ 0 \\ \dot{q}_2 \end{bmatrix} \tag{9}$$

$$w_1 = w_2 = 0 \tag{10}$$

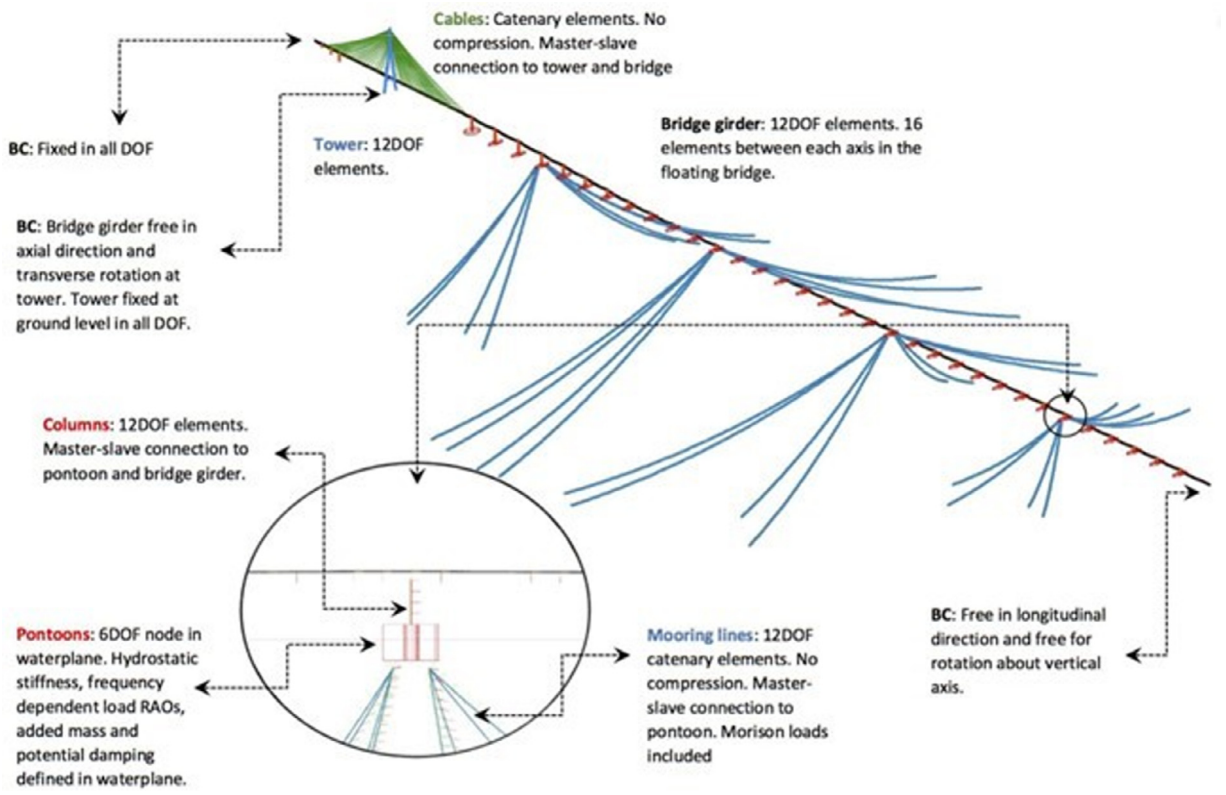

Fig. 8. Environmental analyses overview of the *Orcaflex* model [2].

Total kinetic and potential energy of the system, T and V, respectively can be expressed as:

$$T = \frac{1}{2}\sum_{i=1}^{2}\left(m_i v_i{}^T v_i + w_i{}^T I_i w_i\right) = \frac{1}{2}\begin{bmatrix}\dot{q}_1 & \dot{q}_2\end{bmatrix}\begin{bmatrix}m_1+m_2 & 0\\ 0 & m_2\end{bmatrix}\begin{bmatrix}\dot{q}_1\\ \dot{q}_2\end{bmatrix} \tag{11}$$

$$V = (m_1\ g + m_2\ g)\cdot q_2 + Constant \tag{12}$$

where I is a symmetric 3 3 Inertia tensor matrix. The Lagrangian of the multi-body dynamical system is:

$$L = \sum_{i=1}^{N} T_i - V_i \tag{13}$$

Adams Solver calculates the motion of the multi-body system using the following form of Euler-Lagrange equation [19]

$$\frac{d}{dt}\left(\frac{\partial L}{\partial \dot{q}}\right) - \frac{\partial L}{\partial q} + \phi_q{}^T\lambda = Q \tag{14}$$

where Q is the externally applied non-potential forces in the system, $\phi_q{}^T\lambda$ represents the constraint forces and λ is the column matrix of Lagrange multipliers.

While the popular 2-post or 4-post suspension analysis test rig is typically used for sub-system tests and dynamics analyses where the vehicle is not in forward motion ($v_x = 0$), the investigation in this research requires the vehicle to be in motion ($v_x > 0$) on a road so that aerodynamic loads may be dynamically allowed to interact with the vehicle, thus allowing us to analyze aspects related to vehicle dynamics.

To achieve this, the relation between the tyre contact patch marker on the vehicle and its corresponding reference marker on the ground part (road surface) must be modified, enabling the vehicle to transfer forces on to the ground (reaction part). A macro is enabled in the Adams environment to redefine this relation from the ground reference marker to that on the tyre pad reference marker on the multi-post test rig. This simply shifts the *ground → tyre* interaction to *ground → multi-post rig → tyre* interface. The compound time-history displacements of the bridge motion can be resolved and thus induced on the vehicle when it is in forward motion ($v_x > 0$).

Bridge motion excitation

A detailed dynamic and static structural analyses of the floating bridge finite element model were done using *Orcaflex* and *Sofistik* software respectively [2]. The numerical modelling of the floating bridge on *Orcaflex* is illustrated in (Fig. 8).

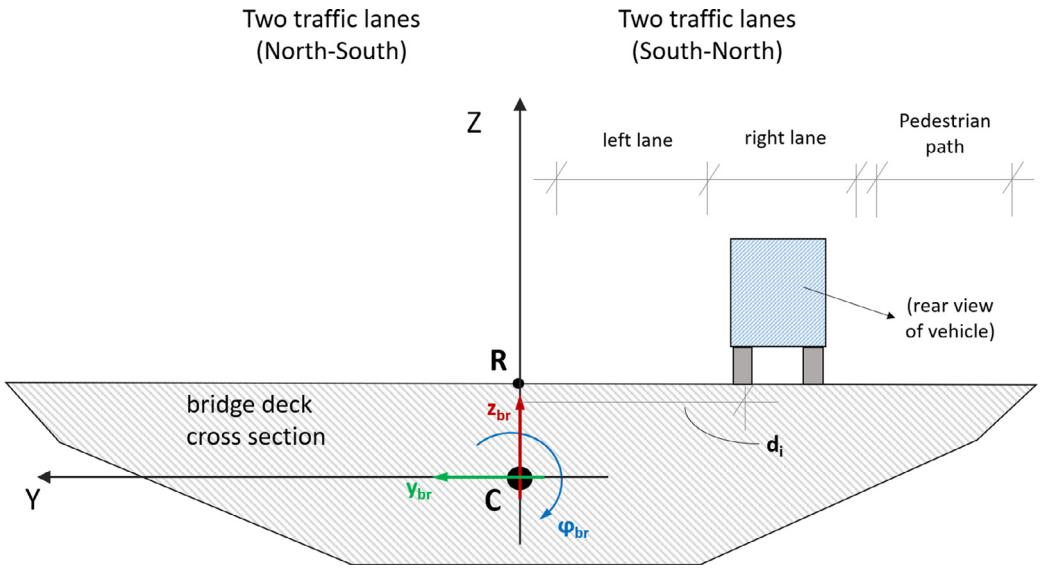

Fig. 9. Bridge deck cross-section.

Finite segment theory is used to describe the structural properties of the line elements used in the bridge model. The results of this method are similar to those obtained by applying finite element beam theory on slender structures. Geometric non-linear stiffness of the model is considered for every static position and time increment. A cable element with zero compression, bending and torsion stiffness is used in modelling the stay-cables and mooring lines. For elements indirectly constrained to each other, a master-slave connection is applied.

The southernmost abutment is rigidly coupled to the bridge girder. The northernmost abutment of the bridge is constrained to allow elongation and rotation about the vertical axis. A fixed joint is considered for rotation, vertical and horizontal translation of the bridge girder at the tower. All elements were defined through a linear material model.

In *Orcaflex*, a stochastic wave field is computed accounting for the wave spreading spectrum and the defined JONSWAP-spectrum. The hydrodynamic loads are applied in the instantaneous position of the bridge pontoons by transforming the wave elevation to loads using the calculated load coefficients in *Wamit*. The loads on the bridge mooring lines are defined using Hydrodynamic Morrison equations. *WindSim* software was used to generate the wind velocity field based on aerodynamic buffeting theory in time domain. All objects above the water surface are subject to wind loads. However, only static wind loads are considered for pontoons. Wind analysis was done on *WindSim* while the response of the marine structures was analysed on *Orcaflex*. More information on *Orcaflex* software is available in [20,21].

The floating bridge motion is simulated for 1 h on *Orcaflex* software, considering the excitation from wind and waves. The bridge motion is obtained in terms of heave (z_{br}), roll (φ_{br}) and lateral (y_{br}) displacements for the bridge deck center (Fig. 9).

This complex motion of the bridge is simplified to a combination of lateral and vertical motion along the length of the bridge. The vertical bridge motion (z_{br}) and the roll motion (φ_{br}) of the bridge are combined as vertical excitation for the left and right wheels for every axle of the vehicle (Eq. 15). Furthermore, the road roughness (ζ_{rr})(ISO8608, road class 'A') [22] and the elevation profile of the bridge (h_{br}) are also included in the combined vertical displacement (ζ_{ti}).

$$\zeta_{ti} = z_{br} + d_i\varphi_{br} + \zeta_{rr} + h_{br} \quad (i = left, right) \tag{15}$$

Fig. 10 a illustrates the combined vertical excitation (ζ_{ti}) for the left and right wheels of the steer axle at 36 km/h. The larger undulation observed in Fig. 10b is as a result of the vertical motion (z_{br}) of the bridge, while the smaller undulation is due to the road roughness (ζ_{rr}). The difference noticed between the two signals is a consequence of the roll motion of the bridge (φ_{br}). Furthermore, the PSD of the combined vertical excitation is illustrated in Fig. 10c. It is observed that the intensity of the signals lie below 0.02 Hz.

The lateral (y_{br}) and combined vertical bridge displacements (ζ_{ti}) are induced on the Adams TS model via the multi-post test rig as described in Section 4.1. The test rig consists of a tyrepad-piston-cylinder system with a translation joint to allow for the vertical bridge displacements (ζ_{ti}). Two such systems are assembled on a base with a translation joint to allow for the lateral bridge displacement (y_{br}) to be induced. This forms a 2-post rig for either wheels of an axle. The base is constrained to the ground with a fixed joint. The 2-post rigs are assembled at each axle location, thus making it a multi-post test rig as illustrated in Fig. 11.

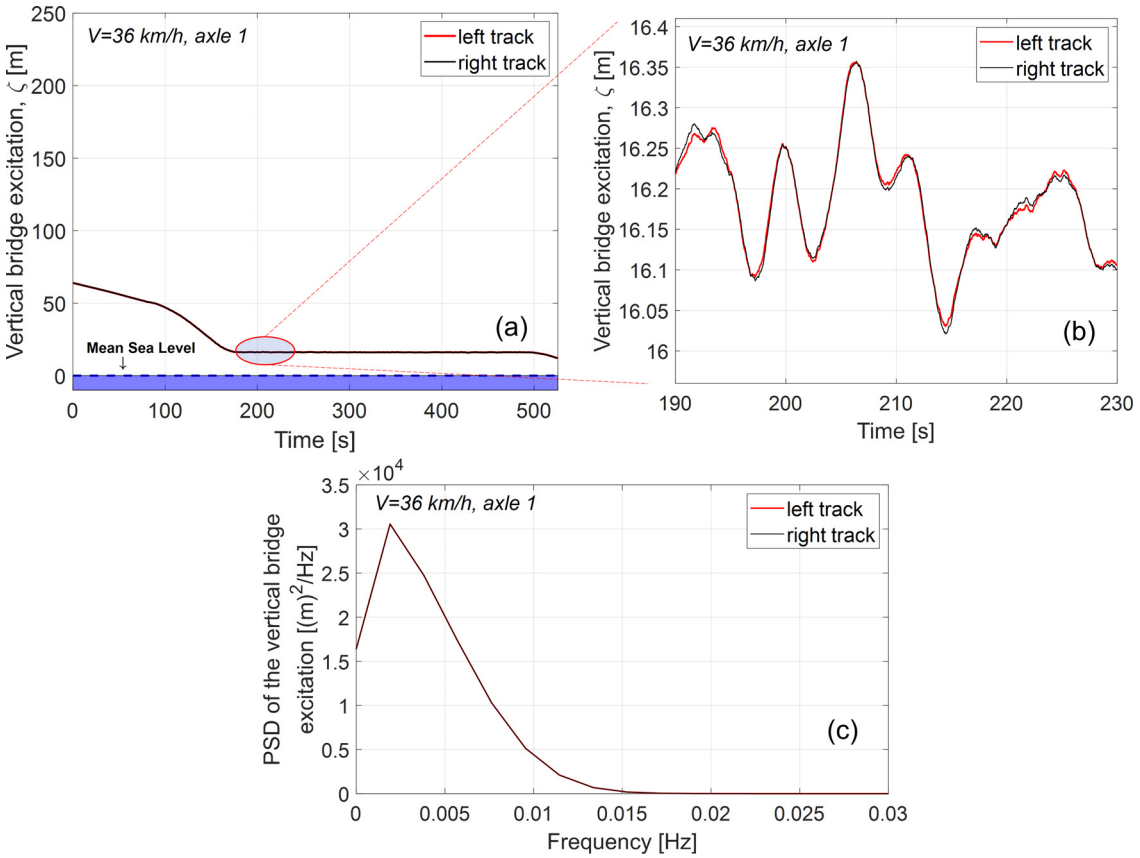

Fig. 10. Vehicle input a) Vertical bridge excitation b) magnified view c) PSD of Vertical bridge excitation, for vehicle speed of 36 km/h.

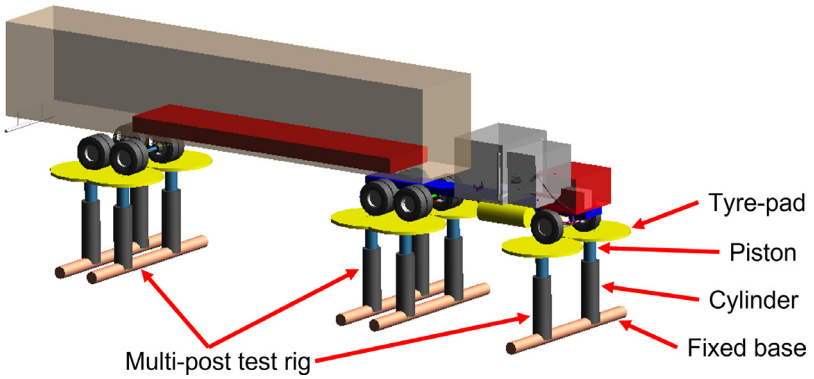

Fig. 11. Adams vehicle model with Multi-post test rig.

4.2. Method to introduce wind excitation

The aerodynamic force and moment coefficients for the TS were determined for a wind yaw angle sweep of 0° to 90° through numerical CFD simulation on STAR CCM+. The effects of articulation between the tractor and semi-trailer units on the aerodynamic coefficients were not considered. The coefficients for the tractor unit were explicitly computed about the axle 1 midpoint projected on the ground and similarly about the axle 4 midpoint projected on the ground for the semi-trailer unit (denoted by yellow stars in Fig. 2). These points are henceforth referred asaerodynamic reference points. The aerodynamic force and moment coefficients are depicted in Fig. 12.

The wind excitation is introduced to each of the tractor and semi-trailer units in the Adams Car Truck as single point forces (GFORCE). The point of application is the CoG of individual vehicle units. The aerodynamic moment coefficients computed about the aerodynamic reference points are transformed to the CoG points through the set of Eq. 16 and Eq. 17 for

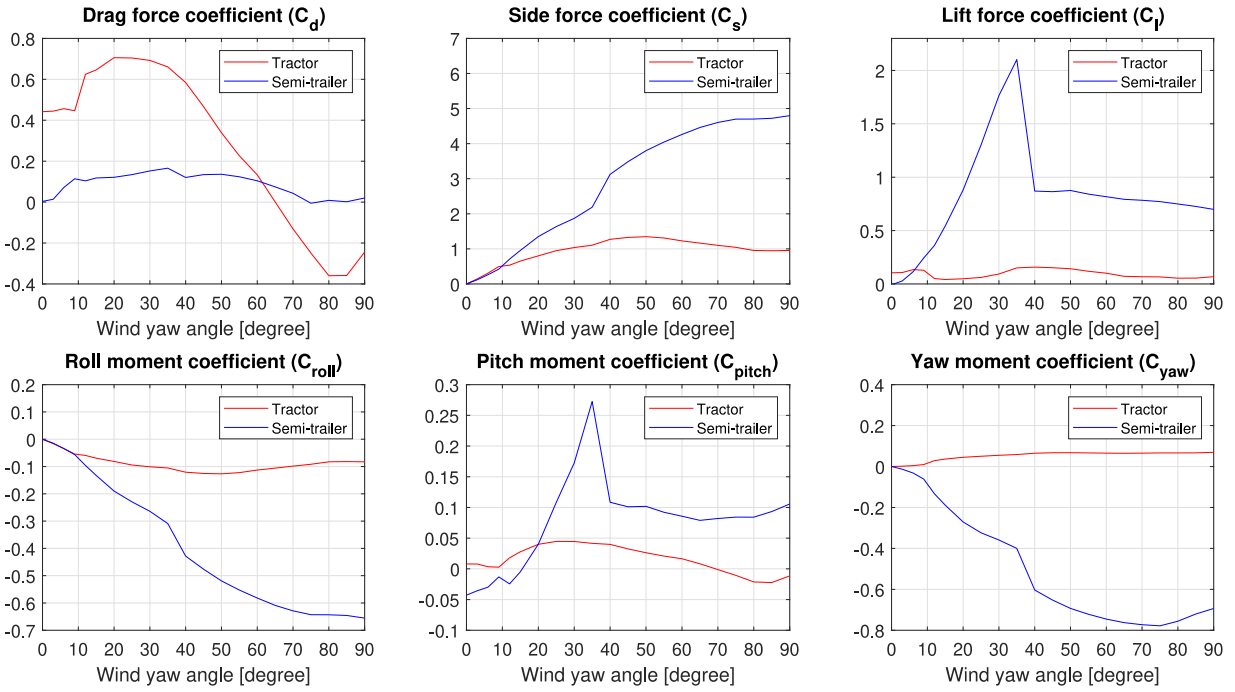

Fig. 12. Aerodynamic force and moment coefficients of the TS model.

the tractor and semi-trailer units respectively.

$$\begin{aligned} c^*_{roll,t}(\beta_{w,t}) &= c_{roll,t}(\beta_{w,t}) + c_{s,t} * \left(\tfrac{h_{CoG,t}-h_{RRC,t}}{L}\right) \\ c^*_{pitch,t}(\beta_{w,t}) &= c_{pitch,t}(\beta_{w,t}) + c_{l,t} * \left(\tfrac{L_{CoG,t}-L_{ref,t}}{L}\right) - c_{d,t} * \left(\tfrac{h_{CoG,t}}{L}\right) \\ c^*_{yaw,t}(\beta_{w,t}) &= c_{yaw,t}(\beta_{w,t}) - c_{s,t} * \left(\tfrac{L_{CoG,t}-L_{ref,t}}{L}\right) \end{aligned} \tag{16}$$

$$\begin{aligned} c^*_{roll,s}(\beta_{w,s}) &= c_{roll,s}(\beta_{w,s}) + c_{s,s} * \left(\tfrac{h_{CoG,s}-h_{RRC,s}}{L}\right) \\ c^*_{pitch,s}(\beta_{w,s}) &= c_{pitch,s}(\beta_{w,s}) - c_{l,s} * \left(\tfrac{L_{ref,s}-L_{CoG,s}}{L}\right) - c_{d,s} * \left(\tfrac{h_{CoG,s}}{L}\right) \\ c^*_{yaw,s}(\beta_{w,s}) &= c_{yaw,s}(\beta_{w,s}) + c_{s,s} * \left(\tfrac{L_{ref,s}-L_{CoG,s}}{L}\right) \end{aligned} \tag{17}$$

where β_w is the wind yaw angle, h_{CoG} is the height of CoG from the ground, h_{RRC} is the vertical distance between the CoG projected on the roll axis and the ground, and L is the vehicle wheelbase (17.5 m). The difference $(h_{CoG} - h_{RRC})$ is the vertical distance between the CoG and roll axis of the respective tractor and semi-trailer units. The difference of L_{ref} and L_{CoG} is the longitudinal distances between the aerodynamic reference points and CoG respective vehicle units (Fig. 2). The subscripts t and s denote tractor and semi-trailer units respectively.

The aerodynamic forces and moments are represented by the equations,

$$\begin{aligned} F_{x,wind} &= \tfrac{1}{2}\rho A V_{rel}^2 c_d(\beta_w) & M_{x,wind} &= \tfrac{1}{2}\rho A L V_{rel}^2 c^*_{roll}(\beta_w) \\ F_{y,wind} &= \tfrac{1}{2}\rho A V_{rel}^2 c_s(\beta_w) & M_{y,wind} &= \tfrac{1}{2}\rho A L V_{rel}^2 c^*_{pitch}(\beta_w) \\ F_{z,wind} &= \tfrac{1}{2}\rho A V_{rel}^2 c_l(\beta_w) & M_{z,wind} &= \tfrac{1}{2}\rho A L V_{rel}^2 c^*_{yaw}(\beta_w) \end{aligned} \tag{18}$$

The relative wind velocity is calculated using the transformation matrix,

$$T_{vehicle,i} = \begin{bmatrix} \cos(\psi_i) & \sin(\psi_i) \\ -\sin(\psi_i) & \cos(\psi_i) \end{bmatrix} \approx \begin{bmatrix} 1 & \psi_i \\ -\psi_i & 1 \end{bmatrix} \tag{19}$$

$$\begin{bmatrix} V_{x,wind} \\ V_{y,wind} \end{bmatrix}_{LCS,i} = T_{vehicle,i} * \begin{bmatrix} -V_{x,wind} \\ -V_{y,wind} \end{bmatrix}_{ECS,i} \tag{20}$$

$$\begin{bmatrix} V_x \\ V_y \end{bmatrix}_{rel,i} = \begin{bmatrix} V_{x,wind} \\ V_{y,wind} \end{bmatrix}_{LCS,i} - \begin{bmatrix} V_x \\ V_y \end{bmatrix}_{vehicle,i} \tag{21}$$

where $T_{vehicle}$ is the coordinate transformation matrix, *LCS* and *ECS* are local and earth coordinate systems respectively, and i denotes the tractor or semi-trailer unit.

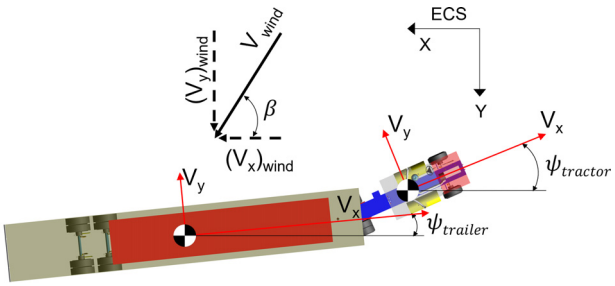

Fig. 13. Relative velocity and wind yaw angle.

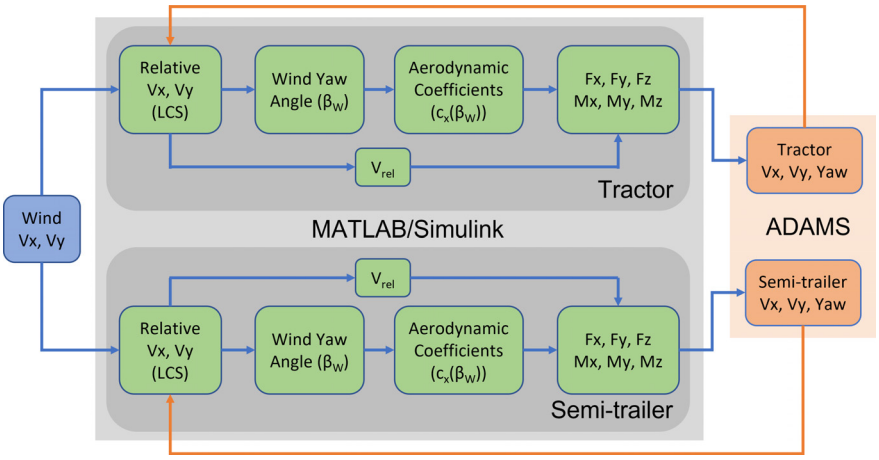

Fig. 14. Co-simulation flowchart for wind excitation.

The magnitude of relative velocity ($V_{rel,wind}$) for individual vehicle units is thereby determined as illustrated in Fig. 13 using Eq. 22,

$$V_{rel,wind,i} = \sqrt{V_{x,rel,i}^2 + V_{y,rel,i}^2} \tag{22}$$

The wind yaw angle (β_w) on each vehicle unit is dynamically calculated by,

$$\beta_{w,i} = \arctan\left(\frac{V_{y,rel,i}}{V_{x,rel,i}}\right) \tag{23}$$

An overview of the co-simulation to determine aerodynamic force and moment in MATLAB/Simulink and use it as GFORCE in Adams TS model is illustrated in Fig. 14.

Wind excitation

The wind data set considered is from the 1-year storm condition simulated on the *WindSim* software. The data obtained is wind velocity along the principal axes. The wind velocity in vertical direction is observed to be of small magnitude and is therefore neglected in this research. The longitudinal and lateral component of wind velocities that the TS (vehicle velocity of 36 km/h and 90 km/h) would experience during the South-North journey on the bridge is illustrated in the Fig. 15a and Fig. 15b. The power spectral density (PSD) of wind velocity is presented in Fig. 15c and Fig. 15d. It can be observed that the wind excitation is of frequencies less than 0.05 Hz.

5. Simulation results and discussion

This section presents the outcomes of the simulations for the laden TS that has been integrated with the newly developed multi-post test rig to incorporate the compound bridge motion to interact with the vehicle. The Adams machine control is used together with the detailed vehicle model that is subjected to the 1-year storm weather condition for four different constant vehicle speeds.

5.1. Path tracking and lateral lane deviation

The path tracking ability of the laden vehicle model at 36 km/h and 90 km/h speeds, along the bridge is presented in Fig. 16. The reference point considered in the driver model is the mid-point of the first drive axle in the tractor unit. It

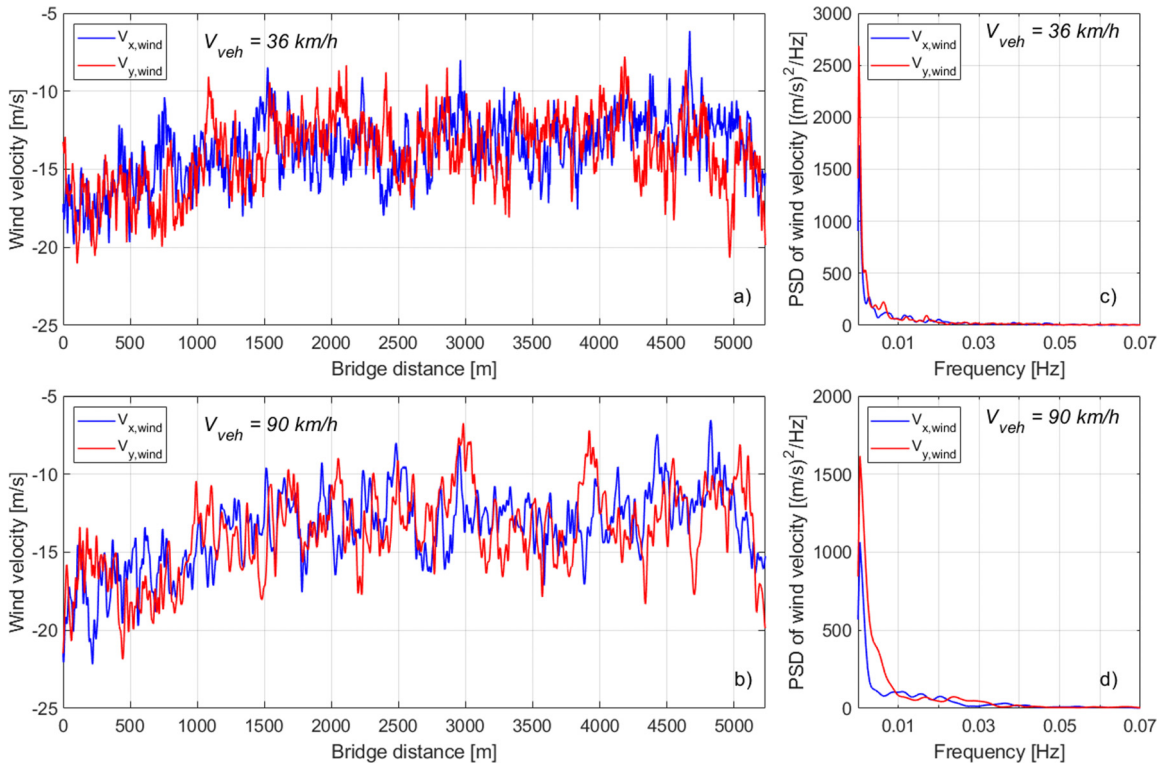

Fig. 15. Wind velocity at vehicle speeds of a) 36 km/h; b) 90 km/h and corresponding PSD of wind velocity at vehicle speeds of c) 36 km/h; d) 90 km/h.

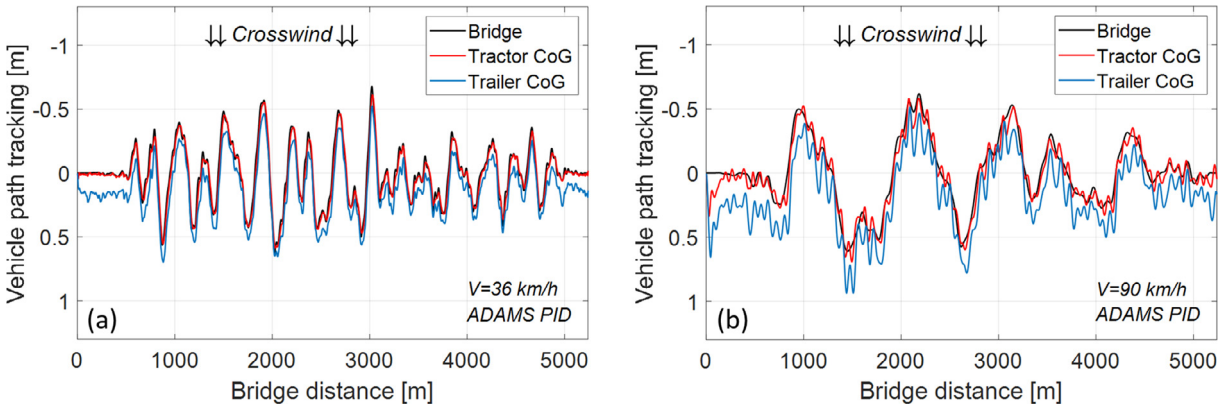

Fig. 16. Path tracking ability of a laden TS a) 36 km/h b) 90 km/h.

is observed that the tractor unit closely follows the intended course on the bridge at 36 km/h, while it follows the path reasonably well at 90 km/h. The lateral offset from the semi-trailer's CoG is a consequence of the effect of crosswind on the second unit and is noticed to be greater at 90 km/h than 36 km/h.

As a consequence of the articulation existing between the tractor unit and the semi-trailer unit, the rear corner points on the semi-trailer are examined to investigate traffic lane violation. Considering a road lane width of 3.6 m, the trace of semi-trailer's rear corner points are depicted in Fig. 17 for a laden case at different vehicle speeds.

The semi-trailer's rear corner points do not violate the lane throughout the course of the bridge at 36 km/h (Fig. 17a), whereas it is observed to violate the lane on multiple occasions at other vehicle speeds. In particular, traffic lane violation for vehicle speeds 54 km/h and 72 km/h is predominantly detected in the first section of the bridge (until around 2000 m), and is not noticed in the remaining section of the bridge (Fig. 17b and Fig. 17c). At 90 km/h however, the semi-trailer's right rear corner is observed to violate the traffic lane on multiple occasions throughout the course of the bridge Fig. 17d).

The maximum lane deviation across vehicle speeds has been summarized in Fig. 18a. The vehicle stays within the lane at 36 km/h, while the rear right corner of the semi-trailer violates the lane for all other vehicle speeds. Lane deviation is

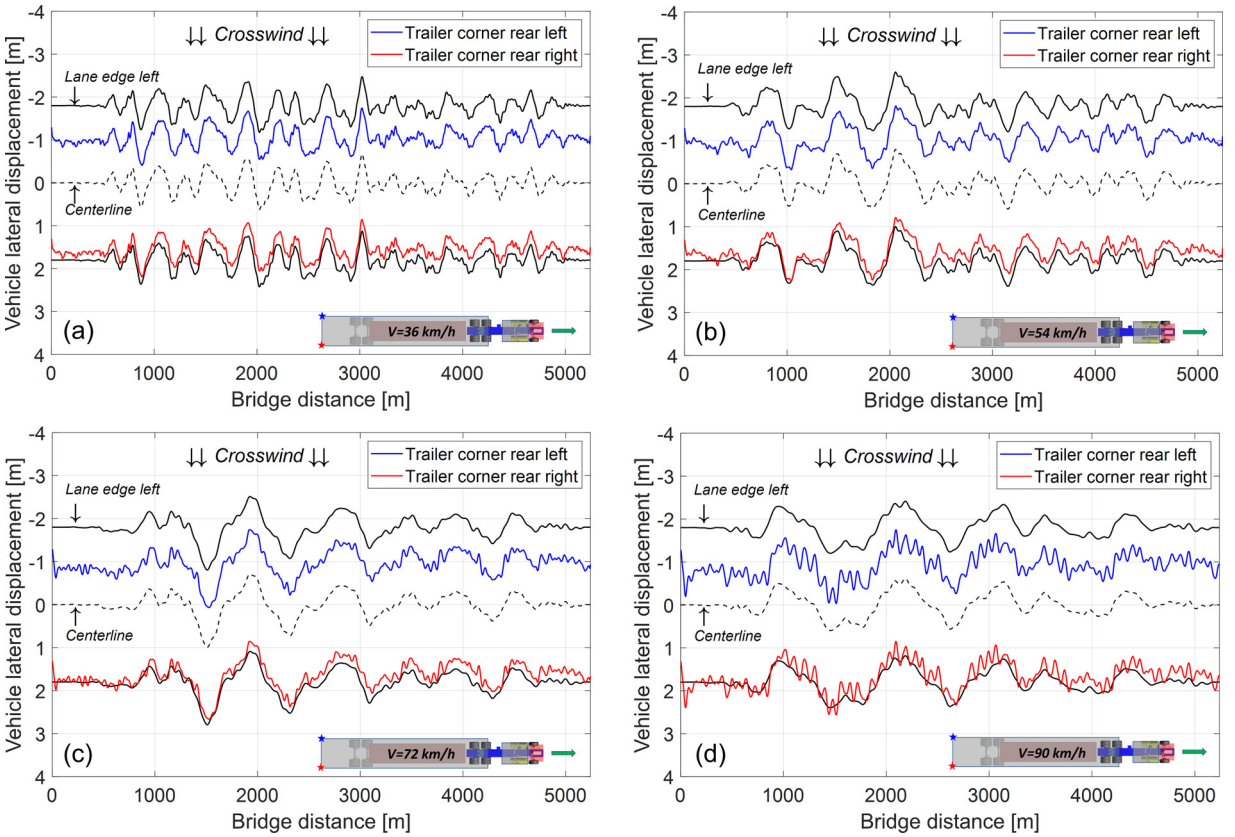

Fig. 17. Traffic lane deviation for a laden TS at speed of a) 36 km/h b) 54 km/h c) 72 km/h d) 90 km/h.

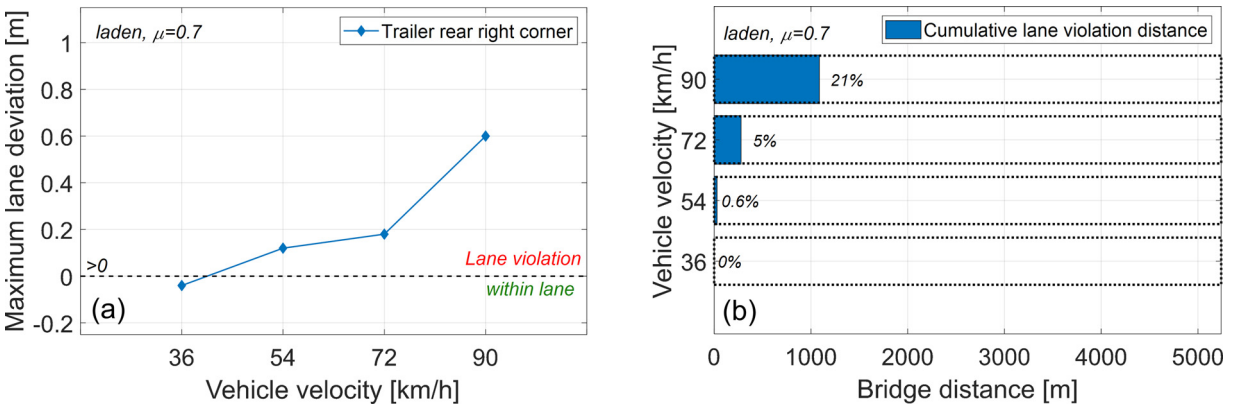

Fig. 18. Summary of lane violation a) maximum lane deviation b) percentage distance of cumulative lane violation.

directly proportional to the vehicle speed, with a maximum deviation of 0.6m at 90 km/h. Furthermore, the lane deviations are substantial at the beginning of the bridge (Fig. 17d).

The cumulative lane violation distance against the length of the bridge for each speed has been illustrated in Fig. 18b. It is observed that the cumulative distance of lane violation is larger with higher vehicle speeds. The vehicle cumulatively violates the lane for a significant distance (21%) at 90 km/h.

5.2. Roll-over risk

Losing contact between one side of the vehicle's wheels on an axle and the bridge deck under the influence of crosswind are particularly susceptible to a roll-over incident of the vehicle. Fig. 19 through Fig. 21 illustrate the vertical tyre forces for each wheel of the leading axles of the tractor semi-trailer at 36 km/h and 90 km/h. The vertical tyre forces of the trailing

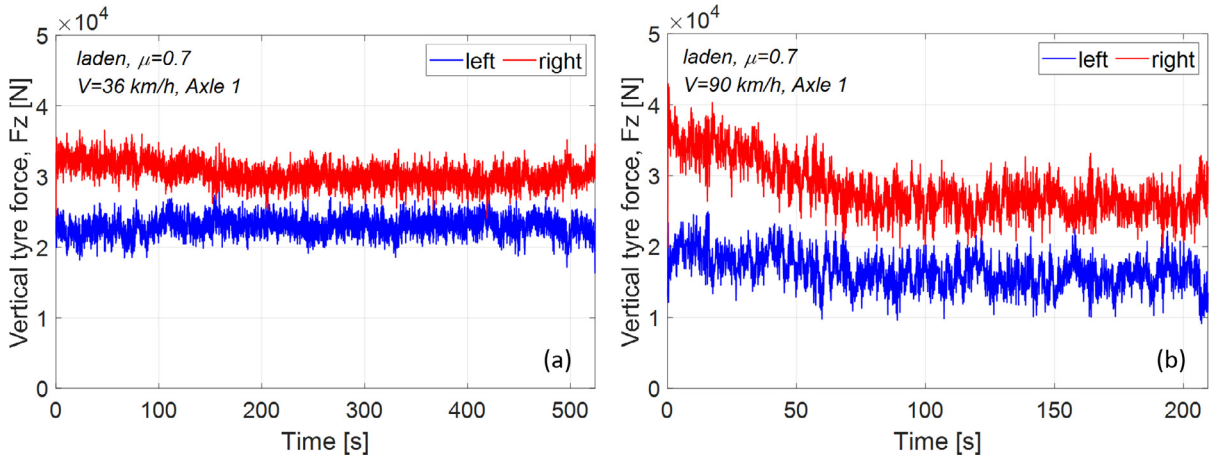

Fig. 19. Vertical tyre forces on axle 1 for a) 36 km/h b) 90 km/h.

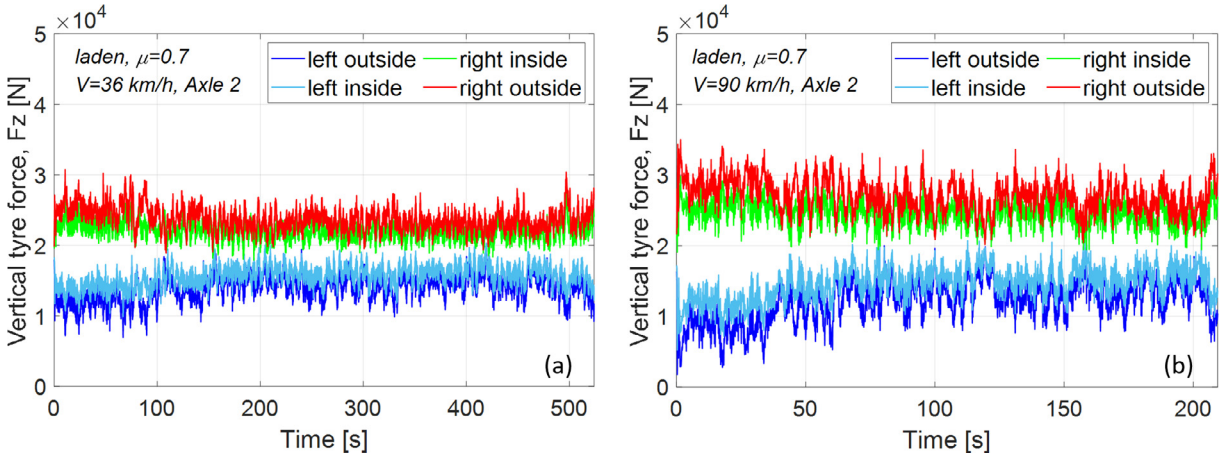

Fig. 20. Vertical tyre forces on axle 2 for a) 36 km/h b) 90 km/h.

axle in both the drive axle group and the semi-trailer axle group are similar to their respective leading axle. The vertical tyre forces on the windward side are noticed to record lower values than the leeward side, signifying a load transfer between the windward wheels and the leeward wheels on an axle. Furthermore, the variation of vertical tyre forces are more volatile and the load transfer is observed to be greater in every axle at a vehicle speed of 90 km/h compared to 36 km/h. As soon as the vehicle enters the bridge at 90 km/h, the vertical tyre force of the windward wheel in axle 4 (Fig. 21b) is observed to be zero, losing contact with the bridge deck and indicating a potential roll-over risk.

High values of the crosswind component (Fig. 15b) in combination with the vehicle longitudinal speed generate wind rolling moments of high magnitude (Fig. 23). A high wind rolling moment in addition to the difference in road roughness between the left and right tracks of the vehicle causes considerable load transfer from windward (left side) to the leeward (right side) wheels. This results in the vertical tyre force values close to zero (Fig. 22).

The Load Transfer Ratio (LTR) indicator is often used to predict potential roll-over occurrences [23]. There are different approaches when it comes to the interpretation of LTR values. The first approach considers the absolute LTR value equal to 1 for one axle or for the whole vehicle as criteria for vehicle rollover. The second approach is stricter and considers the absolute LTR value greater than 0.9 for one axle or for the whole vehicle as the criteria for vehicle rollover. This paper considers the second approach with the absolute value of LTR for one axle greater than 0.9 as the criterion for vehicle overturning according to [24]. It is defined for each axle as

$$LTR_i = \frac{(F_{zl,i} - F_{zr,i})}{(F_{zl,i} + F_{zr,i})} \tag{24}$$

where,

F_{zl} : vertical tyre forces on the left track of the axle
F_{zr} : vertical tyre forces on the right track of the axle
i : axle number (1, ..., 5)

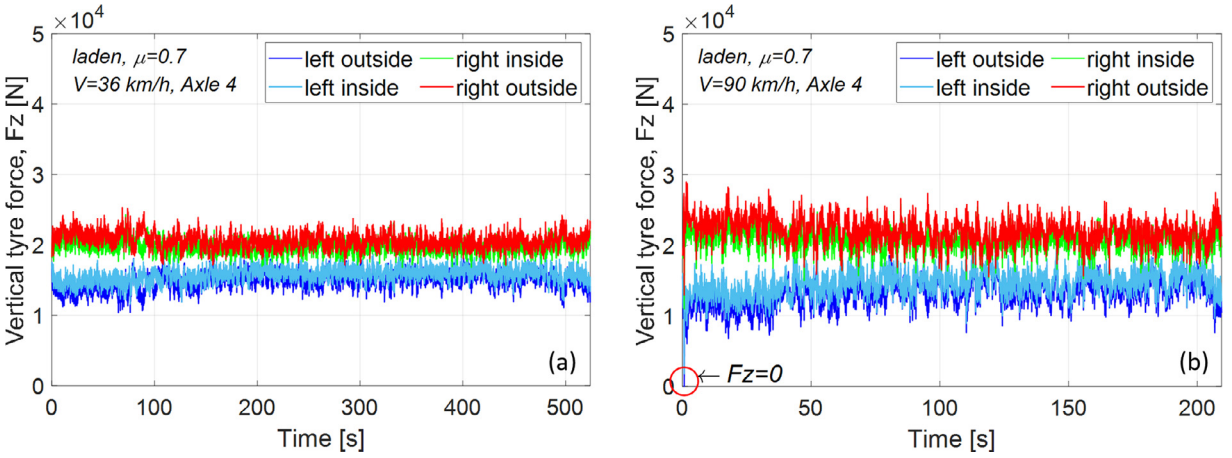

Fig. 21. Vertical tyre forces on axle 4 for a) 36 km/h b) 90 km/h.

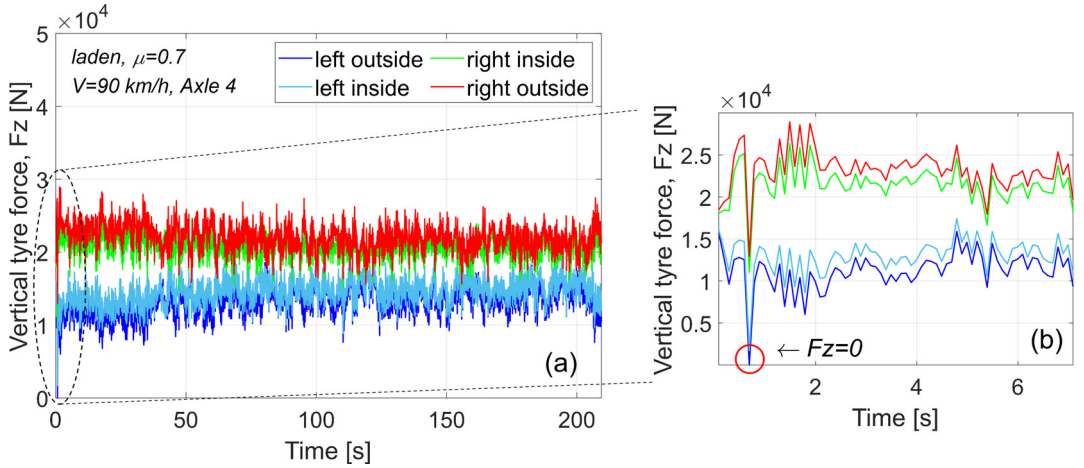

Fig. 22. Vertical tyre forces a) axle 4 at vehicle speed of 90 km/h (Fig. 21b) b) magnified view.

The maximum absolute value of LTR presented in Fig. 24a shows higher values for the case at 90 km/h over 36 km/h on all the axles. Furthermore, the highest LTR value appearing on axle 4 suggests that the roll-over event of the vehicle could begin with wheel lift-off from the semi-trailer axle group. The RMS value of LTR (Fig. 24b) also shows higher values for the case of 90 km/h compared to 36 km/h on every axle. Higher RMS values of LTR on axle 2 and axle 3 implies that the load transfer occurs more often on the tractor's drive axle group compared to other axles.

The relation of the LTR indicator to vehicle speeds across all the axles is summarized in Fig. 25. The maximum absolute LTR values (Fig. 25a) and the RMS values (Fig. 25b) are observed to increase with increase in vehicle speed. This implies greater load transfer and higher likelihood of wheel-off with potential roll-over risk for vehicle speeds at 90 km/h and beyond.

5.3. Risk of losing lateral grip

The Lateral Side-slip Limit (LSL) is based on the criterion that the minimum value of the difference between the maximum allowable friction forces of all wheels and the actual tyre forces should be equal to or greater than zero [25]. The LSL is defined for the every axle in the Eq. 25 [26]:

$$LSL_{axle,k} = min\left(\sqrt{\left(F_{xy}\right)^2 - \left((F_x)^2 + (F_y)^2\right)}\right) = min\left(\sqrt{\left(\mu \cdot F_z\right)^2 - \left((F_x)^2 + (F_y)^2\right)}\right) \quad (25)$$

where F_{xy} is the maximum available friction forces on the respective axle; F_z is the actual vertical force on the respective axle of the vehicle; F_x is the actual longitudinal tyre force on the respective axle; F_y is the actual lateral tyre force on the respective axle; μ is the road friction coefficient; and k is the axle number from 1 to 5. If the minimum LSL value is under zero for a given axle, that particular axle starts to sideslip and lose lateral grip.

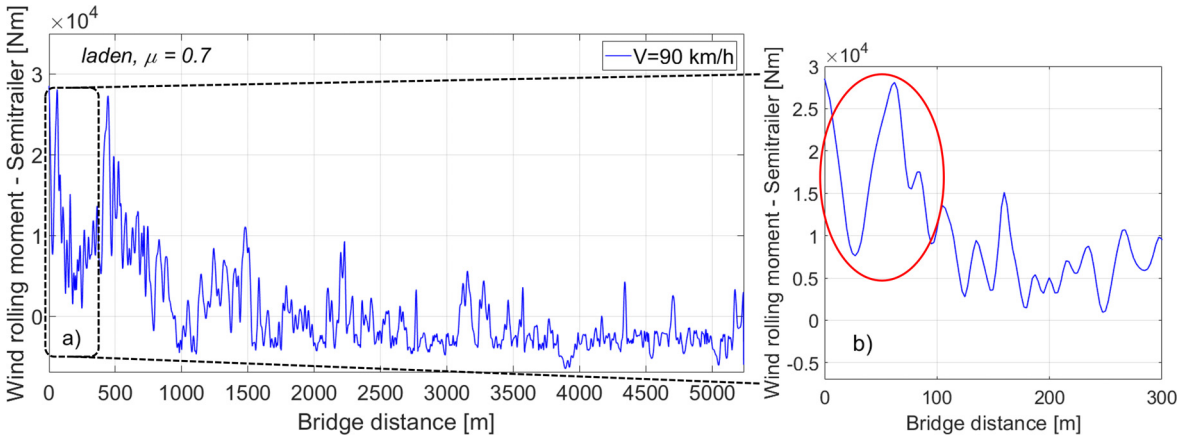

Fig. 23. Wind rolling moment on semi-trailer a) at vehicle speed of 90 km/h b) magnified view.

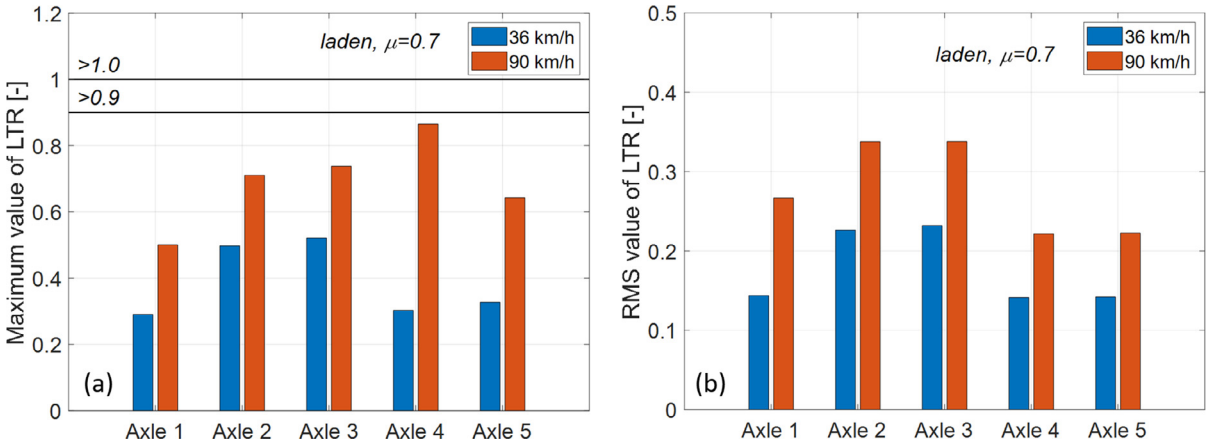

Fig. 24. LTR comparison at 36 km/h and 90 km/h a) Absolute maximum value b) RMS value.

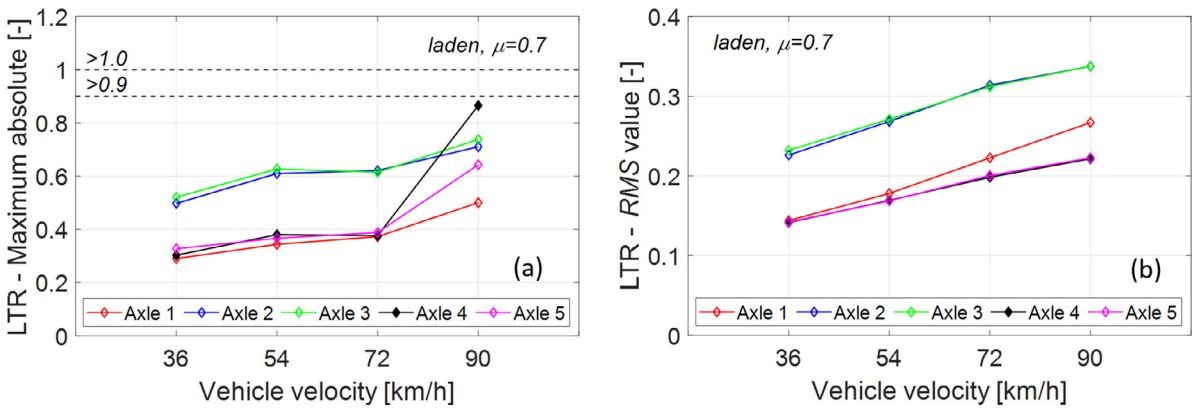

Fig. 25. Summary of LTR across different vehicle speeds a) Absolute maximum value b) RMS value.

Fig. 26 shows the minimum value LSL for every axle, and it is observed to be greater than zero for both the cases, implying that the LSL is not reached. The minimum value of LSL is noted to be lower in every axle for the test case at 90 km/h compared to that at 36 km/h, signifying that the vehicle has lower grip at 90 km/h. The LSL values for the other two vehicle speeds logically lie between 36 km/h and 90 km/h. Furthermore, the trailer-axle group indicates lower minimum LSL values among all double-wheeled axles.

Thus, it follows that greater the vehicle speed, greater is the interaction of aerodynamic loads with the vehicle coupled with the bridge motion. The outcome from all the measures are logical with the performance and integration of the newly

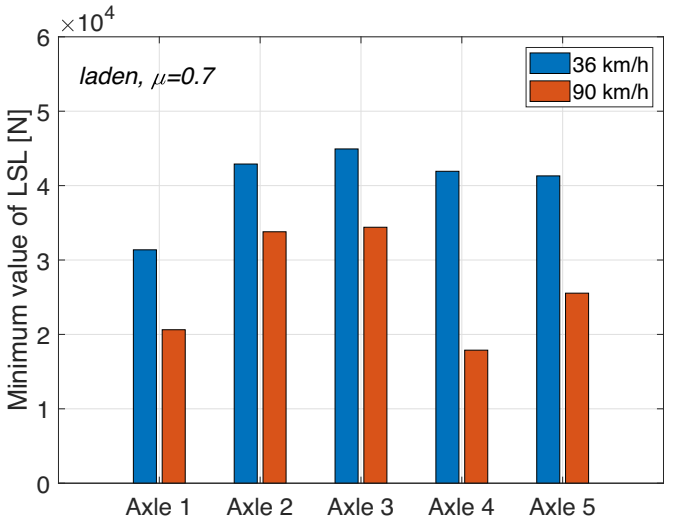

Fig. 26. Minimum value of LSL for every axle at 36 km/h and 90 km/h.

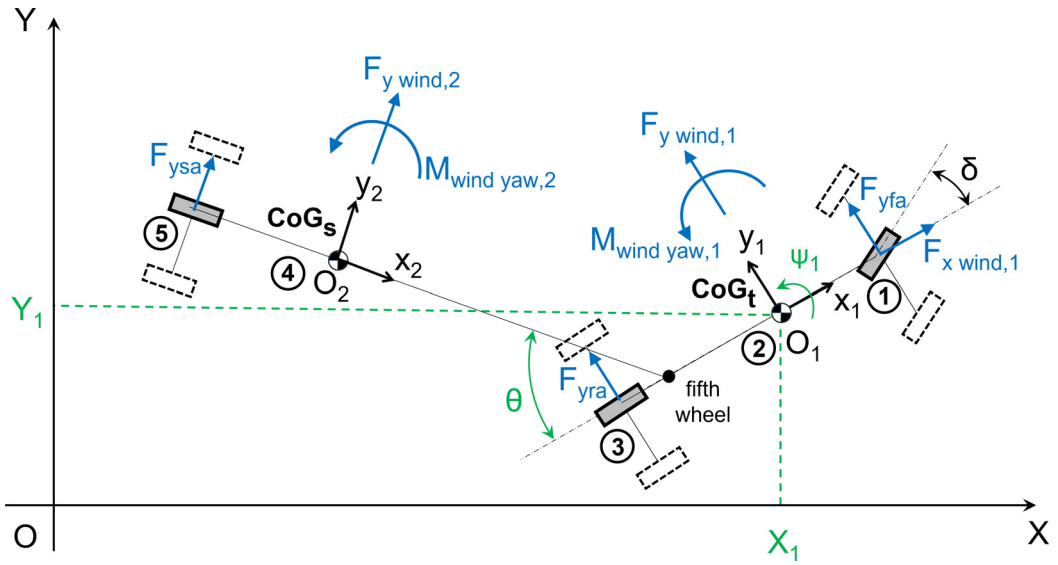

Fig. 27. Vehicle motion in ground plane, aerial view.

developed multi-post test rig and the resolved application of aerodynamic loads on both the vehicle units. The newly established multi-post test rig can be tailored to any road vehicle and this methodology is particularly useful to analyze vehicle dynamics on a moving-ground.

6. MATLAB/Simulink TS model validation

Simulation results from the detailed Adams model will be used in this section to validate the simpler 9 DoF TS model defined in MATLAB/Simulink software and presented in detail in [12]. The DoF in the ground plane are the longitudinal, lateral and yaw motion of the tractor along with the articulation angle (X_1, Y_1, ψ_1 and θ) (Fig. 27). The DoF out-of-ground-plane are the roll motions of the unsprung mass of the tractor and the semi-trailer, the front and rear axle of the tractor, and the semi-trailer's axle (ϕ_1, ϕ_2, ϕ_{fa}, ϕ_{ra}, and ϕ_{sa}) (Fig. 28). On account of the very long wavelengths of the vertical displacements of the bridge, the pitch motion of the tractor and the semi-trailer have been discounted. Furthermore, owing to the low vertical excitation frequencies of the bridge deck, the vertical motion of the tractor and the semi-trailer have been disregarded [12]. The bridge deck's lateral velocities (V_{ybr} in Fig. 28) at the tyre contact points of the front, rear and semi-trailer axles have been used to calculate the lateral tyre forces.

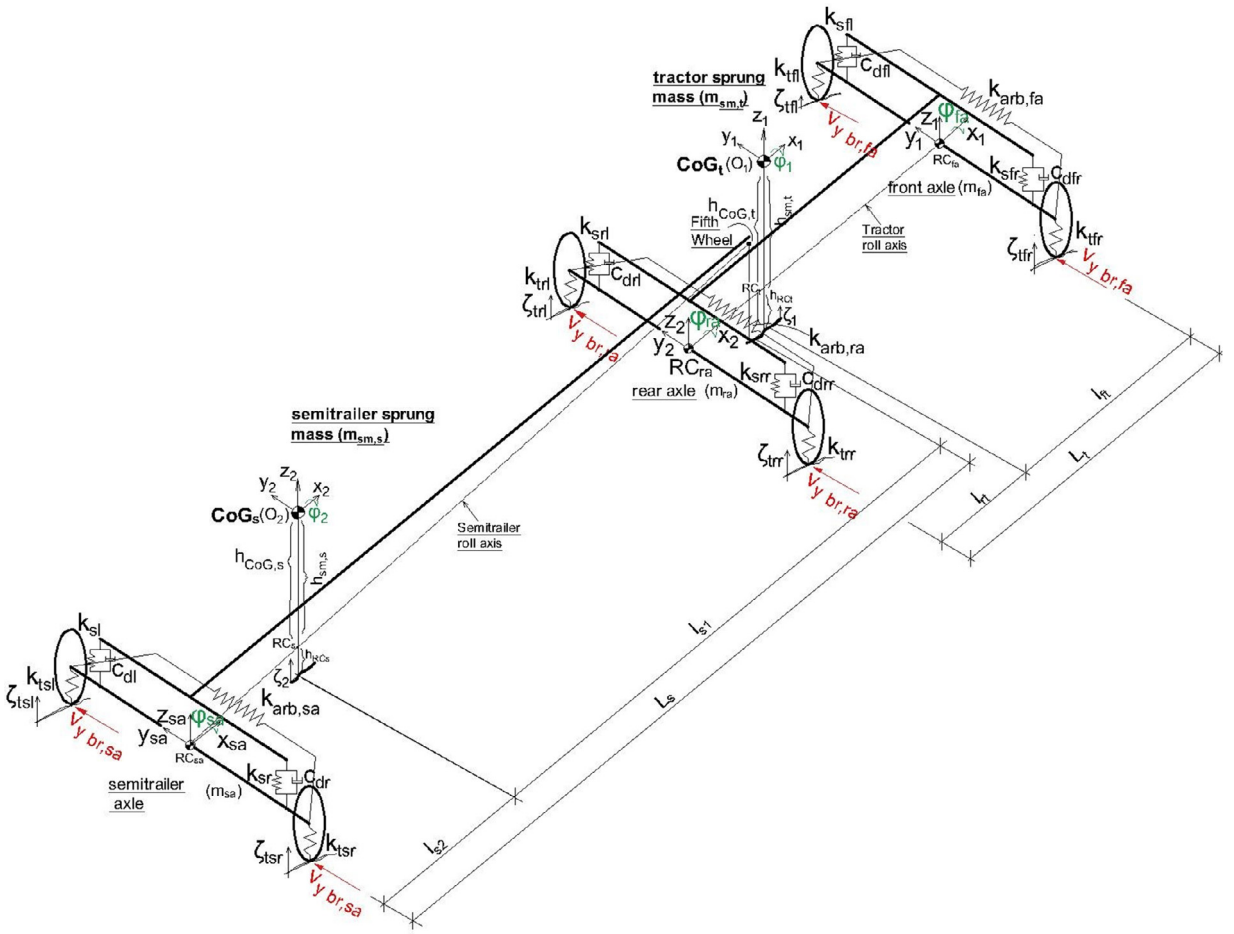

Fig. 28. Vehicle parameters and out-of-ground-plane motion.

A TS model consisting of three rigid axles and 9 DoF was defined by Lagrangian method. The method is notably advantageous when modelling vehicles involving multiple units. Contrary to Newtons technique, a Lagrangian formulation does not include reaction forces at the fifth wheel, thus resulting in fewer equation terms to handle. Lagrangian formulation was applied (Eq. 26) when formulating non-linear differential equations of motions.

$$\frac{d}{dt}\left(\frac{\partial T}{\partial \dot{q}_i}\right) - \frac{\partial T}{\partial q_i} + \frac{\partial V}{\partial q_i} + \frac{\partial D}{\partial \dot{q}_i} = Q_i \quad (i = 1, 2, \ldots, n) \tag{26}$$

where T, V, D, q_i, $\dot{q}_i$, Q_i and n are the kinetic, potential, dissipative energy of the system, generalized coordinates, generalized velocities, generalized forces and total number of generalized coordinates, respectively.

The generalized coordinates of the system are

$$q = \left[X_1, Y_1, \psi_1, \theta, \phi_1, \phi_2, \phi_{fa}, \phi_{ra}, \phi_{sa}\right]^T \tag{27}$$

The kinetic energy of the rigid bodies from the in-ground-plane and out-of-ground-plane motion constitute the kinetic energy of the system. The spring deformation (tyres, and air springs in the suspension system), variations in the CoG height of sprung mass caused by roll motion and deformation of the anti-roll bar together account for the potential energy of the system. Dampers in the suspension system represent the dissipative energy of the system. The detailed derivation of the equations for the kinetic energy, the potential energy and the dissipative energy can be found in [12].

Generalized forces are given by

$$Q_i = \sum_{j=1}^{k} \left(\frac{\partial \dot{r}_j}{\partial \dot{q}_i}\right) \cdot F_j \quad (i = 1, 2, \ldots, n), \quad \dot{q} = \left[u, v, \dot{\psi}_1, \dot{\theta}, \dot{\phi}_1, \dot{\phi}_2, \dot{\phi}_{fa}, \dot{\phi}_{ra}, \dot{\phi}_{sa}\right]^T \tag{28}$$

where Q_i, $\dot{r}_j$ and F_j are generalized forces, velocity vectors of the points where external forces act (Fig. 27), and external tyre and wind forces (Fig. 27), respectively. Lagrangian equations were derived using MATLAB code written by the authors where Simulink blocks for every generalized coordinate serves as the output. These blocks are then used for the TS model definition.

Table 4
Geometric parameters of the tractor/semitrailer unit.

Parameter	Notation	Value
Wheelbase of tractor	L_t	5.95 m
Distance between the tractor's CoG and its front axle	l_{ft}	3.00 m
Distance between the tractor's CoG and its rear axle	l_{rt}	2.95 m
Height of the tractor's CoG from the ground	$h_{CoG,t}$	1.16 m
Wheelbase of semi-trailer	L_s	11.6 m
Distance between the fifth wheel and the semi-trailer's CoG	l_{s1}	9.18 m
Distance between the semi-trailer's CoG to the semi-trailer axle	l_{s2}	1.19 m
Height of the semi-trailer's CoG from the ground	$h_{CoG,s}$	1.724 m
Wheelbase of the tractor semi-trailer combination	L_{TS}	20.51 m

Table 5
Mass parameters of the tractor/semitrailer unit.

Parameter	Notation	Value
Sprung mass of tractor	$m_{sm,t}$	8739 kg
Mass of tractor's front axle	m_{fa}	746 kg
Mass of tractor's rear axle	m_{ra}	1355 kg
Moment of inertia of tractor's sprung mass about its x-axis	$J_{t,x}$	15,000 kgm^2
Moment of inertia of tractor about its z-axis	$J_{t,z}$	21,500 kgm^2
Unladen semi-trailer's sprung mass	$m_{sm,s}$	8100 kg
Mass of equivalent axle of semi-trailer	m_{sa}	1800 kg
Moment of inertia of semi-trailer's sprung mass about its x-axis	$J_{s,x}$	85,500 kgm^2
Moment of inertia of semi-trailer about its z-axis	$J_{s,z}$	151,000 kgm^2

Table 6
Oscillatory parameters of the tractor/semitrailer unit.

Parameter	Notation	Value
Spring stiffness of single air spring on the tractor's front axle	k_{sfl}, k_{sfr}	175,000 N/m
Damping coefficient of single shock-absorber on the tractor's front axle	$c_{d,fa}$	20,000 Ns/m
Damping coefficient of equivalent shock-absorber on the tractor's front axle	c_{dfl}, c_{dfr}	40,000 Ns/m
Spring stiffness of single air spring on the tractor's rear axle	$k_{s,ra}$	200,000 N/m
Spring stiffness of equivalent air spring on the tractor's rear axle	k_{srl}, k_{srr}	400,000 N/m
Damping coefficient of single shock-absorber on the tractor's rear axle	$c_{d,ra}$	22,500 Ns/m
Damping coefficient of equivalent shock-absorber on the tractor's rear axle	c_{drl}, c_{drr}	45,000 Ns/m
Radial tyre stiffness of single tyre on the tractor's front axle	k_{tfl}, k_{tfr}	1,000,000 N/m
Radial tyre stiffness of equivalent tyre on the tractor's rear axle	k_{trl}, k_{trr}	4,000,000 N/m
Air spring stiffness of single spring on the semi-trailer axle	$k_{s,sa}$	200,000 N/m
Air spring stiffness of equivalent spring on the semi-trailer axle	k_{sl}, k_{sr}	400,000 N/m
Damping coefficient of single shock-absorber on the semi-trailer axle	$c_{d,sa}$	22,500 Ns/m
Damping coefficient of equivalent shock-absorber on the semi-trailer axle	c_{dl}, c_{dr}	45,000 Ns/m
Radial tyre stiffness of single tyre on the semi-trailer axle	k_{tfl}, k_{tfr}	1,000,000 N/m
Radial tyre stiffness of equivalent tyre on the semi-trailer axle	k_{tsl}, k_{tsr}	6,000,000 N/m
Torsional stiffness of anti-roll bar on tractor's front axle	$k_{arb,fa}$	120,000 Nm/rad
Torsional stiffness of anti-roll bar on tractor's rear axle	$k_{arb,ra}$	120,000 Nm/rad
Torsional stiffness of anti-roll bar on semi-trailer axle	$k_{arb,sa}$	120,000 Nm/rad

Vehicle parameters (e.g. mass, moment of inertia, spring and damper characteristics, etc.) of the MATLAB/Simulink TS model has been adjusted to match the parameters of the Adams TS model. One equivalent axle was considered instead of dual-wheeled tandem drive axles for the tractor unit. Similarly, one equivalent axle in place of two dual-wheeled axles was considered for the semi-trailer axle. Brush tyre model has been used in MATLAB/Simulink TS model as compared to the PAC2002 tyre model in Adams TS model. In the validation process, signals from different measures (tyre vertical forces, vehicle path deviation and HSA) for three different vehicle speeds (36 km/h, 54 km/h and 72 km/h) have been considered. The case of an unloaded vehicle and a road friction of 0.7 is studied for the validation process. Tables 4, 5 and 6 enumerate the vehicle parameters mentioned in Fig. 28.

6.1. Path tracking

Fig. 29 comparatively shows path tracking for the both vehicle models at 36 km/h. It can be seen that the position of the tractor and semi-trailer CoGs with respect to the path are quite similar for both vehicle models.

Fig. 30 comparatively shows the RMS and absolute value of maximal lateral deviation of the vehicle's path against the three vehicle speeds. It can be pointed out that the values are almost identical for the tractor at 54 km/h, while at 36 km/h

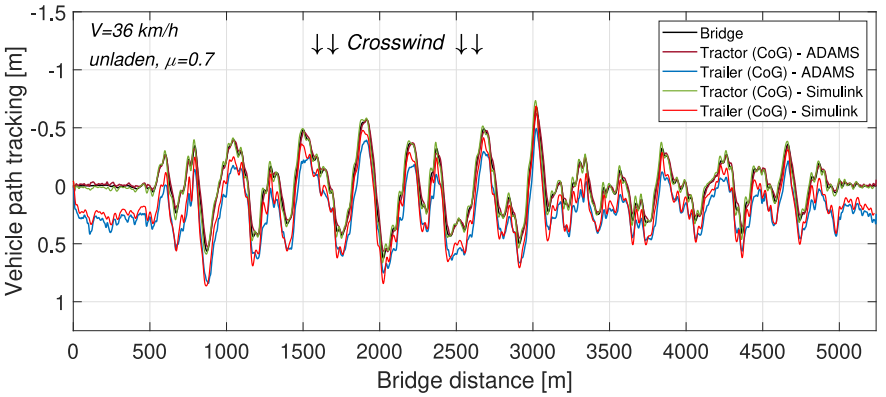

Fig. 29. Vehicle path tracking for both vehicle models.

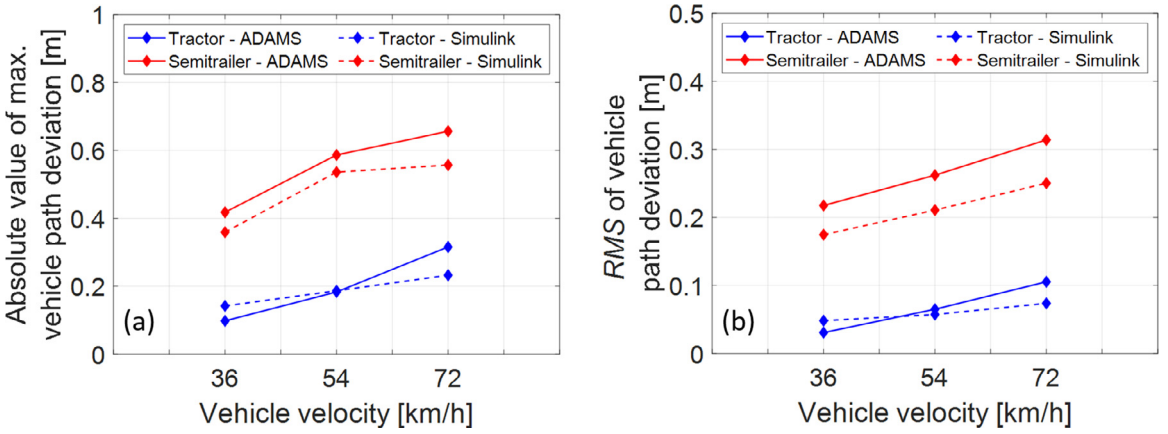

Fig. 30. Vehicle path deviation a) absolute value of maximal deviation; b) RMS value.

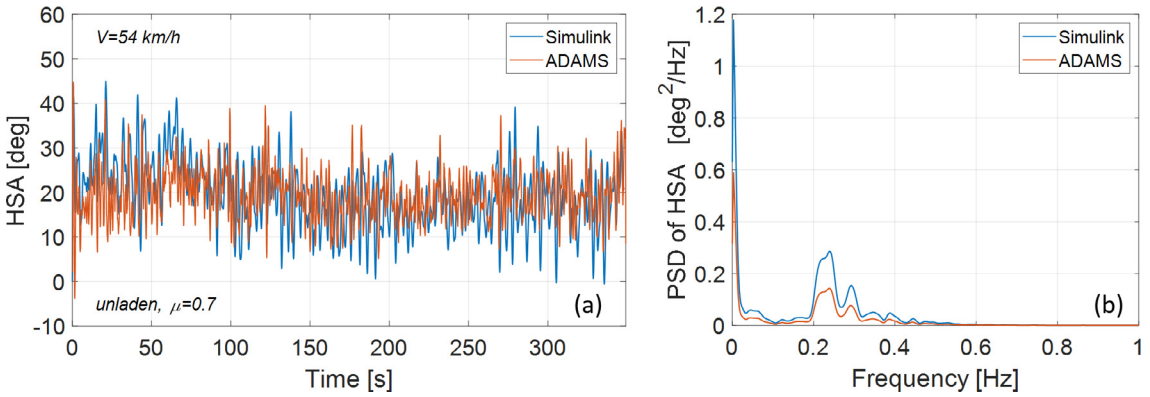

Fig. 31. HSA signals in a) time domain; b) frequency domain.

and 72 km/h the differences are minor. For the semi-trailer, marginally higher values are noticed for the Adams vehicle model.

6.2. Hand wheel steering angle

Fig. 31 comparatively presents HSA signals for both vehicle models for speed of 54 km/h. The magnitudes of both HSA signal are similar (Fig. 31a). Intensities of the both signals are concentrated around two frequency ranges; one below 0.05 Hz and the other, around 0.25 Hz (Fig. 31b). HSA from MATLAB/Simulink vehicle model has slightly higher intensities in com-

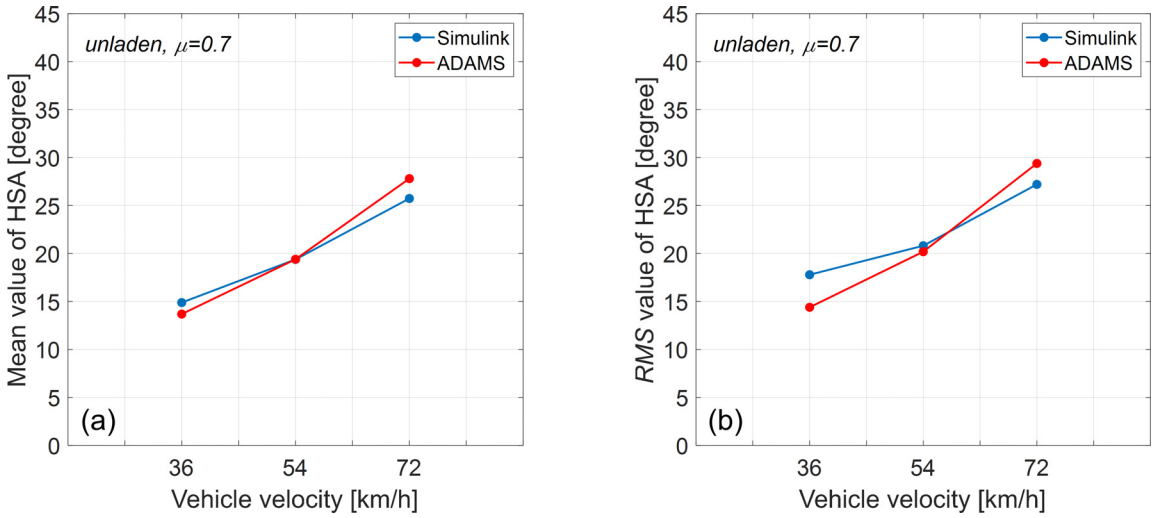

Fig. 32. HSA signals a) Mean value b) RMS value.

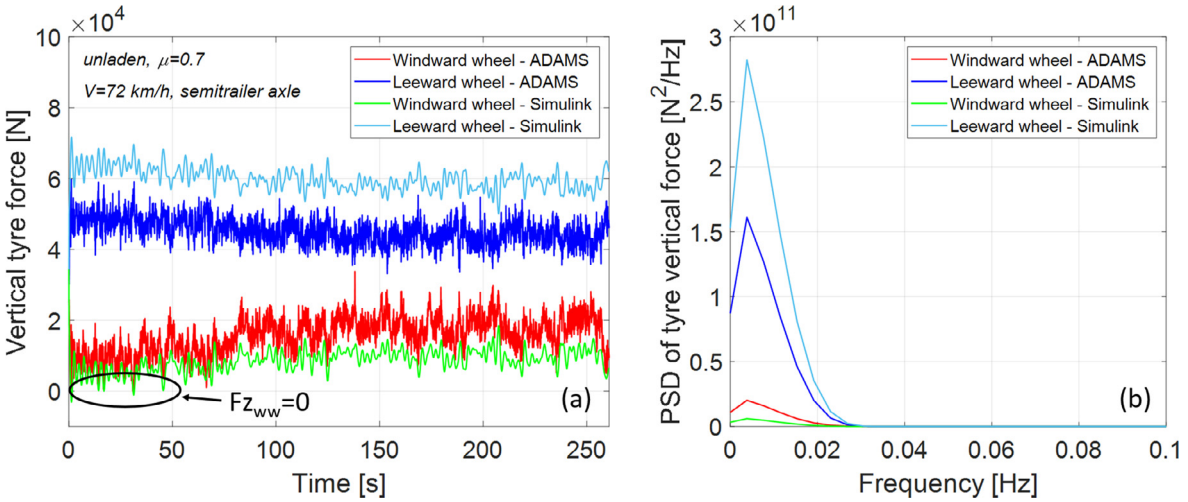

Fig. 33. Vertical tyre forces for semi-trailer axle in a) time domain; b) frequency domain.

parison with the Adams model. Similar conclusions have been confirmed with the signals for the speed of 36 km/h and 72 km/h.

Fig. 32 compares the RMS and the mean value of HSA from both the vehicle models. The mean value for both signals are quite similar, whereas the RMS value slightly differs at 36 km/h.

6.3. Roll-over risk

Fig. 33 comparatively illustrates the normal tyre forces of the semi-trailer axle for both vehicle models at 72 km/h. The magnitudes of tyre forces from the MATLAB/Simulink TS model are higher than those from Adams model (Fig. 33a). Nevertheless, values of the windward tyres forces are fairly similar for the first 50 seconds of simulation time which is important when it comes to vehicle's roll-over risk assessment. Higher intensities of the vertical tyre forces for MATLAB/Simulink TS model can be also seen in the frequency domain (Fig. 33b). These findings could be attributed to modelling differences pertaining to tyre model, single-wheeled single axle (versus dual-wheeled tandem axle in the Adams model), and fewer DoF, among others.

7. Conclusion

In this research, methods to incorporate the bridge motion and to introduce wind excitation on the built-in TS model in Adams Car Truck software were developed. The methods enabled investigation of lateral dynamics for a laden TS exposed

to floating bridge and wind excitation for a 1-year storm condition. Based on the simulation results from Adams software, simpler TS model built in MATLAB/Simulink software had been validated. The main conclusions from this research are as follows:

1. The method to introduce floating bridge motion excitation includes a multi-post test-rig modelled as a Cartesian manipulator which has a vertical and horizontal displacement. Two translation (prismatic) joints are used in order to model the vertical, horizontal, and roll excitation of the bridge on each vehicle wheel. The method to introduce wind excitation is based on co-simulation to determine aerodynamic forces and moments in MATLAB/Simulink and use it as GFORCE in Adams TS model. Simulation results showed the effectiveness of the developed methods.
2. The lateral lane deviation of the vehicle is influenced by vehicle speed, aerodynamic load, and bridge motion excitation. The lane deviation magnitude follows a positive correlation with vehicle speed. As soon as the vehicle accesses the bridge, the high-intensity crosswind component interacts with the vehicle resulting in a significant lane deviation. The maximum lane deviation is around 0.6 m at 90 km/h. The percentage of lane violation occurring along the length of the bridge is also higher at higher vehicle speeds.
3. Vertical tyre forces of the windward wheels have lower values than those of the leeward wheels as a consequence of lateral load transfer due to crosswinds interacting with the vehicle. Within the first few seconds of the simulation, the windward outer wheel of the leading semi-trailer axle ceases contact with the road surface of the bridge deck, indicating potential risk of vehicle roll-over at 90 km/h.
4. Lane violation and roll-over risk are significantly high when the vehicle enters the bridge through to the descending section. Therefore, it is suggested that the bridge entry speed be limited to 36 km/h until the vehicle reaches the lower section of the bridge (around 2 km) before proceeding to maintain a maximum vehicle speed of 72 km/h.
5. The methods can be customized to suit investigation of vehicle dynamics for road vehicles (eg. buses, passenger cars, etc.) on diverse bridges such as suspension bridges or floating bridges.
6. The path tracking ability and path deviation of the MATLAB/Simulink TS model are comparable to the Adams TS model for an unladen case at 36 km/h. At 54 km/h, the HSA signals are similar between the models in both time and frequency domains.
7. The vertical tyre force values from the MATLAB/Simulink model are observed to follow the trend of the values obtained in the Adams model at 72 km/h. The windward vertical tyre force values are fairly similar for the first 50 seconds of simulation time which is important when it comes to vehicle's roll-over risk assessment.
8. Although some of the results from the MATLAB/Simulink model moderately differ from that of the Adams model, they agree rather well for the most part. This outcome is a consequence of the modelling approximations in the MATLAB/Simulink model compared to that of the detailed Adams model. The reduction in model-fidelity allows for a trade-off between the accuracy of the results and simulation time (30 to 70 times faster). This provides flexibility to use the models based on the application needs depending on the scope of investigation.

The Bjørnafjorden floating bridge is part of the coastal highway route E39 Norway's road project, and is currently in its design phase. Therefore, experimental investigation of the vehicle's behaviour and verification of the validity of vehicle models on the Bjørnafjorden floating bridge are planned for future work. In addition, measurement of floating bridge motion and crosswind speed along the length of the bridge are planned as future work.

Data Availability

Data will be made available on request.

Acknowledgement

The Norwegian Public Roads Administration (NPRA) has rendered invaluable support for this research, which is gratefully acknowledged. Additionally, the resources provided by the Swedish National Infrastructure for Computing (SNIC) were utilized to perform aerodynamic simulations.

References

[1] K. Dunham, Coastal highway route E39 extreme crossings, Transp. Res. Procedia 14 (2016) 494–498, doi:10.1016/j.trpro.2016.05.102. Transport Research Arena TRA2016
[2] Vegvesen, Analysis and design (base case) Bjørnafjorden, straight floating bridge phase 3 analysis and design (base case), SBJ-31-C3-MUL-22-RE-100 (2017).
[3] T. Moan, M. Eidem, Floating bridges and submerged tunnels in norway the history and future outlook, Springer Singapore 41 (2020) 81–111, doi:10.1007/978-981-13-8743-2_5.
[4] A. Prakash, P. Sivaramakrishnan, Investigation of heavy vehicle dynamics behaviour under the wind and bridge motion excitation, Chalmers Univ. Technol. (2021). https://hdl.handle.net/20.500.12380/303671.
[5] J. Zhu, W. Zhang, M. Wu, Evaluation of ride comfort and driving safety for moving vehicles on slender coastal bridges, ASME. J. Vib. Acoust. 140 (5) (2018). 051012
[6] K. Nguyen, A. Camara, O. Rio, L. Sparowitz, Dynamic effects of turbulent crosswind on the serviceability state of vibrations of a slender arch bridge including wind-vehicle-bridge interaction, J. Bridge Eng. 22 (11) (2017). 06017005

[7] W. Guo, Y. Xu, Safety analysis of moving road vehicles on a long bridge under crosswind, ASCE. J. Eng. Mech. 132 (4) (2006), doi:10.1061/(ASCE)0733-9399(2006)132:4(438).
[8] D. Sekulic, B. Jacobson, S. Johannesen, E. Svangstu, Effect of floating bridge motion on vehicle ride comfort and road grip, in: The IAVSD International Symposium on Dynamics of Vehicles on Roads and Tracks, Springer, 2019, pp. 1416–1424.
[9] D. Sekulic, A. Vdovin, B. Jacobson, S. Sebben, S. Johannesen, Effects of wind loads and floating bridge motion on intercity bus lateral stability, J. Wind Eng. Ind. Aerodyn. 212 (2021) 104589, doi:10.1016/j.jweia.2021.104589. https://www.sciencedirect.com/science/article/pii/S0167610521000751.
[10] A. Gustafsson, C. Svensson, I. Berg, J. Johnsson, M. Lubell, Driver influence on vehicle track-ability on floating bridges. bachelors thesis in mechanical engineering, Chalmers Univ. Technol. (2019).
[11] A. Bhat, A. Naik, C. Reddy, K. Pishey, M. Venkatesh, N. Bharadwaj, Driver influence on vehicle track-ability on floating bridges, Automot. Eng. Proj. Chalmer. Univ. Technol. (2020).
[12] D. Sekulic, A. Vdovin, B. Jacobson, S. Sebben, S. Johannesen, Analysis of vehicles path tracking ability and lateral stability on a floating bridge under crosswind, J. Wind Eng. Ind. Aerodyn. 227 (2022) 105070, doi:10.1016/j.jweia.2022.105070. https://www.sciencedirect.com/science/article/pii/S0167610522001726.
[13] S. Chen, C. Cai, Accident assessment of vehicles on long-span bridges in windy environments, J. Wind Eng. Ind. Aerodyn. 92 (12) (2004) 991–1024.
[14] S. Li, S. Yang, L. Chen, Investigation on cornering brake stability of a heavy-duty vehicle based on a nonlinear three-directional coupled model, Appl. Math. Model. 40 (13–14) (2016) 6310–6323.
[15] Y. Lu, S. Yang, S. Li, L. Chen, Numerical and experimental investigation on stochastic dynamic load of a heavy duty vehicle, Appl. Math. Model. 34 (10) (2010) 2698–2710.
[16] J. Snider, et al., Automatic steering methods for autonomous automobile path tracking, Robotics Institute, Pittsburgh, PA, Tech. Rep. CMU-RITR-09-08 (2009).
[17] M. ADAMS, Car Truck documentation (2019).
[18] M. Spong, S. Hutchinson, M. Vidyasagar, Robot Modelling and Control, 2nd edition, John Wiley & Sons (2004).
[19] J. McConville, J. McGrath, Introduction to adams theory, mechanical dynamics, Inc., paper (1998).
[20] Vegvesen, Bjørnafjorden, straight floating bridge phase 3 analysis and design (base case) appendix a - global structural model and static analysis, SBJ-31-C3-MUL-22-RE-101 (2017).
[21] Vegvesen, Bjørnafjorden, straight floating bridge phase 3 analysis and design (base case) appendix b - environmental loads analysis, SBJ-31-C3-MUL-22-RE-102 (2017).
[22] ISO 8608, Mechanical vibration-road surface profiles-reporting of measured data, 1995.
[23] R. Kamnik, F. Boettiger, K. Hunt, Roll dynamics and lateral load transfer estimation in articulated heavy freight vehicles, Proc. Inst. Mech. Engineer., Part D: J. Automobile Eng. 217 (11) (2003) 985–997.
[24] F. Cheli, P. Belforte, S. Melzi, E. Sabbioni, G. Tomasini, Numerical-experimental approach for evaluating cross-wind aerodynamic effects on heavy vehicles, Veh. Syst. Dyn. 44 (sup1) (2006) 791–804.
[25] F. Chen, S. Chen, Reliability-based assessment of vehicle safety in adverse driving conditions, Transp. Res. Part C: Emerg. Technol. 19 (1) (2011) 156–168.
[26] B. Jacobson, Vehicle Dynamics Compendium, Chalmers University of Technology (2020).